Title

Cofilactin rod formation mediates inflammation-induced neurite degeneration

Journal

Cell Reports, 43(3)

ISSN

2639-1856

Authors

Uruk, Gökhan
Mocanu, Ebony
Shaw, Alisa E
et al.

Publication Date

2024-03-01

DOI

10.1016/j.celrep.2024.113914

Peer reviewed

Cofilactin rod formation mediates inflammation-induced neurite degeneration.

Authors: Gökhan Uruk[1,2], Ebony Mocanu[1,2], Alisa E. Shaw[3], James R. Bamburg[3], *Raymond A. Swanson[1,2]

Affiliations:

[1]Department of Neurology, University of California, San Francisco, San Francisco, CA, USA

[2]Neurology Service, San Francisco Veterans Affairs Health Care System, San Francisco, California, USA.

[3]Department of Biochemistry and Molecular Biology, Colorado State University, Fort Collins, CO, USA

*Raymond A. Swanson. Email: Raymond.Swanson@ucsf.edu

Summary

Stroke, trauma, and neurodegenerative disorders cause loss of neurites (axons and dendrites) in addition to neuronal death. Neurite loss may result directly from a primary insult, secondary to parental neuron death, or secondary to a post-injury inflammatory response. Here we use lipopolysaccharide and the alarmin S100β to selectively evaluate neurite loss caused by the inflammatory response. Activation of microglia and infiltrating macrophages by these stimuli causes neurite loss that far exceeds neuronal death, both in vitro and in vivo. Neurite loss is accompanied by the formation of cofilactin rods and aggregates (CARs), which are polymers of cofilin-1 and actin induced by oxidative stress and other factors. Mice deficient in either cofilin-1 or the superoxide-generating enzyme NOX2 show reduced CAR formation, neurite loss, and motor impairment. The findings identify a mechanism by which inflammation leads to neurite loss via CAR formation and highlight the relevance of neurite loss to functional impairment.

INTRODUCTION

Brain microglia and macrophages (M/M) respond to pro-inflammatory stimuli with an innate immune response that includes the release of cytokines, chemokines, proteases, and reactive oxygen species [1-3]. This response provides a rapid first-line reaction to infection and trauma but can itself injure neighboring neurons and other cell types. The capacity for this response to cause neuronal death is well-established and shown to contribute to a variety of neurological disorders, including Alzheimer's disease, Parkinson's disease, and secondary injury following stroke and brain trauma [1,4-6]. By contrast, far less is known about inflammation-induced injury to neurites, i.e. neuronal axons and dendrites [3].

Neurite degeneration can result from the formation of rod-shaped bundles of cofilin-saturated F-actin, termed cofilactin rods (CARs), as well as other cofilin-containing aggregates [7-10]. Cofilin-1, the ubiquitous mammalian member of the actin depolymerizing factor (ADF)-cofilin family, is best known for regulating the dynamic turnover of actin filaments by severing and depolymerizing F-actin. However, cofilin-1 also binds cooperatively along F-actin and can lead to stable cofilactin filaments, which subserve cytoskeletal functions such as the formation of growth cone filopodia [11,12]. The events leading to pathological CAR formation involve the activation of cofilin-1 by dephosphorylation of its serine-3 residue and the formation of cofilin dimers through intermolecular disulfide bonds [13-15]. CAR formation causes local disruption of cytoskeletal dynamics in neurites, such as anterograde and retrograde trafficking [16-18]. Importantly, this process can occur in the absence of parent neuron demise.

CARs can be identified by immunostaining as focal, rod-shaped aggregates of cofilin-1 and have been observed in animal models of Alzheimer's disease, stroke, and other conditions [10,18,19]. More amorphous coflin-1-containing aggregates are also observed under conditions that form CARs and may represent higher-order polymers, CARs rendered extracellular after neurite degeneration, or other types of cofilin-1 aggregates [10,20]. In fixed brain tissue it is often difficult to colocalize CARs and CAR-related aggregates exclusively to neurites because the cytoskeleton markers for neurites are lost at sites of CAR formation, but in cell culture studies it is clear that these form in neuronal processes and, to a lesser extent, neuronal cell bodies [20,21]. CARs and related cofilin-1 aggregates induced by brain ischemia do not co-localized with CNPase, GFAP, CD11b, or CD31, suggesting that they do not form in brain oligodendrocytes, astrocytes, microglia/macrophages, or endothelium [21].

A potential link between the innate immune response and CAR formation is the oxidative stress produced by activated microglia and infiltrating macrophages (M/M) [22]. M/M and other immune cells markedly increase superoxide and nitric oxide production in response to pro-inflammatory stimuli [23,24]. These stimuli include both exogenous factors such as bacterial lipopolysaccharide and the release of endogenous compounds termed "alarmins", such as the normally intracellular proteins S100β and HMGB1 [25-29]. The production of superoxide and nitric oxide leads in turn to oxidative stress through

the formation of highly reactive oxygen species such as hydrogen peroxide, peroxynitrite, and hydroxyl radical. Oxidative stress drives CAR formation in two ways: by activating phosphatases that dephosphorylate cofilin-1 at its serine-3 residue, and by forming disulfide linkages between cofilin-1 molecules [21,22,30].

These factors suggest that the innate immune response might be a factor driving CAR formation and neurite degeneration. Here we evaluated this possibility in mouse cortex and primary cultures. Our findings show that inflammation causes neurite degeneration far out of proportion to neuronal death and that the neurite degeneration results from CAR formation in response to M/M superoxide production.

RESULTS

S100β induces cofilactin rod formation and subsequent neurite loss

We used Thy1-YFP mice to visualize neuronal cell bodies, axons, and dendrites of mice in which the alarmin S100β was stereotaxically injected into primary motor cortex. These mice developed a dose- and time-dependent loss of neurites, as assessed by measures of both neurite length and neurite area (Fig. 1). By contrast, there was near-complete sparing of neuronal cell bodies over the range of S100β doses used (Fig. 1C). Neuronal cell body survival was also confirmed in a separate set of experiments with wild-type (WT) mice, using NeuN to identify neuronal cell nuclei. In these studies, there was no discernible loss of neuronal nuclei at time points up to two weeks after S100β injections (Suppl. Fig. 1A). There was also no detectable reduction in neuronal nuclear size, as would be expected with incipient cell death [31,32] (Suppl. Fig. 1B-F).

To determine if the neurite loss was associated with the formation of CARs, we used immunostaining for aggregated cofilin-1 [16,21]. In these and subsequent studies, we used WT rather than YFP - expressing mice because the broad fluorescence emission of YFP limits the use of other fluorescent markers. Focal, rod-like aggregates of cofilin-1 indicative of CAR formation were observed in the brains injected with S100β, along with other more amorphous cofilin-1 aggregates (Fig. 2A, B). As previously described, neurofilament integrity was lost at sites of CAR formation, and the CARs often formed linear patterns corresponding to the lost or degenerating neurites [20,21]. CAR formation was maximal by one day after the S100β injections (Fig. 2B-E) and was followed by subsequent neurite loss as assessed by both total neurite length (Fig. 2F-I) and neurite area (Suppl. Fig. 2). Mice injected with 50 ng of denatured (boiled) S100β did not exhibit any increased CAR formation, neurite loss, or M/M activation relative to saline-injected controls (Suppl. Fig. 3).

CAR formation and neurite loss is attenuated in cofilin-1 hemizygous and p47^{phox} deficient mice.

To confirm a causal relationship between CAR formation and neurite loss, we employed cofilin-1 hemizygous ($COF^{-/+}$) mice, which express reduced levels of cofilin-1 (Suppl. Fig. 4) and consequently have reduced propensity for CAR formation [33]. $COF^{-/+}$ mice injected with S100β showed strikingly attenuated formation of CARs (Fig. 3A-D). Importantly, these mice also showed no detectable loss of neurites (Fig. 3E-H) supporting a requisite role for CARs in the inflammation-induced neurite degeneration.

NADPH oxidase-2 (NOX2) is the major source of superoxide released by M/M, and thus a likely source of the oxidative stress driving CAR formation. We therefore, compared the effects of S100β injection in wild-type and $p47^{phox-/-}$ mice, which cannot form an active NOX2 complex. Neuronal oxidative stress was confirmed by immunostaining for γH2AX, which accumulates at foci of DNA strand breaks, in neurons near activated M/M in the WT but not $p47^{phox-/-}$ mice (Suppl. Fig. 5). As expected, the $p47^{phox-/-}$ mice also showed both reduced CAR formation and neurite loss relative to WT mice (Fig. 3).

Functional impairment caused by S100β injection is attenuated in both $COF^{-/+}$ and $p47^{phox-/-}$ mice.

Motor dysfunction in mice following S100β injections into cortex was evaluated using the corner test, which has been widely adopted as a sensitive measure of mouse forelimb impairment [34]. These studies used the same S100β injection dose (50 ng) and location (right primary motor cortex) as used in the histology studies. WT mice showed an increased propensity to turn to the left after S100β but not vehicle (saline) injections, with normalization by day 7 after the injection. By contrast, neither the $COF^{-/+}$ or $p47^{phox-/-}$ mice exhibited motor impairment at any time point evaluated (Fig. 4A, B). Importantly, both the $COF^{-/+}$ mice and $p47^{phox-/-}$ mice showed the same robust M/M response to S100β injections as observed in WT mice (Fig. 4C-F), and in all three mouse genotypes there was no negligible neuronal loss after the 50 ng S100β injections (Suppl Fig. 1).

To determine whether CAR formation with subsequent neurite loss is specific to S100β or a more general consequence of the innate immune response, we also injected mouse cortices with lipopolysaccharide (LPS) at a dose found to have minimal effect on neuronal cell body survival (Fig. 5). The LPS injections likewise induced CAR formation and neurite loss, though the magnitude of these effects was less than observed with S100β.

Roles of microglial NOX2 and neuronal cofilin-1 in inflammation-induced neuronal loss

We used mixed glial / neuronal cell culture preparations to characterize the interactions between these cell types that may drive inflammation-induced neurite loss. The cultures were comprised of WT or $COF^{-/+}$ neurons plated onto a glial layer

(containing astrocytes and microglia) derived from either WT or p47$^{phox-/-}$ mice. (Suppl. Fig. 6). In cultures containing WT neurons and WT glia, S100β produced a dose- and time-dependent induction of CARs (Supp. Fig. 7). The CARs were restricted to the neurites and often caused an abrupt discontinuity of the microtubular cytoskeleton, as identified by immunostaining for microtubule-associated protein-2 (MAP-2). The CAR formation was followed by a similar dose-dependent loss of neurites in these cultures (Suppl. Fig. 8). This neurite loss was not attributable to neuronal death, as inferred by propidium iodide exclusion (Suppl. Fig. 6), thereby indicating a preferential loss of the neuronal processes.

To confirm that the reduced CAR formation and neurite loss observed in COF$^{-/+}$ mouse brain was attributable specifically to decreased expression of cofilin-1 in neurons, we evaluated S100β-induced CAR formation in cultures containing COF$^{-/+}$ neurons and WT glia. These studies showed markedly reduced CAR formation at each of the time points evaluated: 4, 24, and 48 hours (Fig. 6), indicating a requisite role for neuronal cofilin-1 in the neurite loss. We then used cultures containing WT neurons plated onto p47$^{phox-/-}$ glia to confirm that neurite loss was dependent upon glial (rather than neuronal) NOX2 activation. As expected, CAR formation in these cultures was markedly reduced relative to neurons plated onto WT glia at all time points examined (Fig. 6). The reduced CAR formation in cultures containing COF$^{-/+}$ neurons or p47$^{phox-/-}$ glia was accompanied by a parallel reduction in neurite loss (Fig. 7A-D, Suppl. Fig. 9)

DISCUSSION

Pro-inflammatory microglial and macrophage activation contributes to neurological disorders ranging from brain trauma to Alzheimer's disease, but its effects on neuronal axons and dendrites are poorly characterized. The present studies show that axons and dendrites are particularly vulnerable to inflammatory injury. These studies also identify a mechanism by which inflammation-induced neurite injury occurs. Stimuli such as S100β released by damaged cells or lipopolysaccharide from bacterial membranes induce pro-inflammatory M/M responses, which include of NOX2 - mediated superoxide production and recruitment of circulating or perivascular macrophages to the area of tissue damage [35-38]. The resulting oxidative stress on nearby neurites leads to CAR formation, which in turn leads to neurite degeneration and motor dysfunction (Fig. 7E).

Prior evidence that CAR formation leads to neurite loss comes most definitively from studies using forced overexpression of cofilin-1, as cofilin-1 overexpression promotes CAR formation in the absence of other recognized cytotoxic processes [17]. In primary neuron cultures, cofilin-1 overexpression causes CAR formation and subsequent neurite degeneration likely by occluding normal anterograde and retrograde trafficking [15,17,30,39]. Our findings further support a causal role for CARs in neurite loss by showing inflammation-induced neurite loss is markedly reduced in neurons haploinsufficient in cofilin-1, both in cell culture and in vivo.

Our observations that CAR formation was also blocked in mice deficient in p47^{phox}, an essential component of the activated NOX2 complex, confirms a role for superoxide production and oxidative stress in CAR formation and subsequent neurite degeneration. CAR formation requires both dephosphorylation of its serine-3 residue and the formation of cofilin dimers through intermolecular disulfide bonds [13-15], both of which are promoted by oxidative stress. Serine-3 is dephosphorylated by the slingshot phosphatase SSH-1L [40], which is normally sequestered to the scaffolding protein 14-3-3 but is released upon oxidation of 14-3-3ζ [22]. Oxidative stress also promotes the intermolecular disulfide bonding between the cofilin-1 cysteines 39 and 147 that is thought to stabilize CARs [11,14]. Our additional observation that S100β - induced CAR formation and neurite loss largely prevented in the co-cultures containing glia from p47$^{phox-/-}$ mice argues against a requisite role for neuronal NOX2 in these processes; however, neuronal NOX2 activation has been identified as a requisite step in CAR formation induced by a cellular prion protein-dependent pathway [41].

Neurite loss not attributable to parent neuron death has been identified in brain ischemia [42,43] brain trauma [44,45], neurodegenerative disorders [18,33], and sepsis [46,47]. Here, the observations that inflammation-induced neurite loss occurred independently of parent neuronal cell demise was confirmed using both YFP and immunolabeled cells, and in both cell cultures and mouse brain. Most of these studies used S100β and LPS at concentrations titrated to induce neurite loss in the absence of neuronal cell body loss. We considered the possibility that the neurite loss observed 1 - 3 days after S100β injection might simply be a precursor or sign of incipient neuronal death, but found no detectable loss of neurons or reduction in neuronal nuclear size at time points up to 14 days after the injections.

We chose S100β as the inflammatory stimulus because it is an endogenous alarmin that is released by injured cells in conditions such a stroke and trauma and thought to be a major driver of the innate immune response in those conditions [23,27,28]. The similar results obtained using LPS indicate that the greater vulnerability of neurites to inflammatory injury is not unique to the S100β stimulus. The larger effects observed with S100β are consistent with the relative effects of S100β and LPS on microglial activation in vitro [28].

Mouse motor dysfunction was evaluated using the corner test, which has been widely adopted for this purpose [34]. WT mice with S100β injected into motor cortex showed significant impairment while the COF$^{-/+}$ or p47$^{phox-/-}$ mice did not, in agreement with the histological measures of neurite loss. Recovery with time after the injections is difficult to interpret, given the multiple processes known to contribute to recovery after injury to motor cortex. Nevertheless, the motor impairment induced by inflammation in the absence of neuronal cell loss highlights the relevance of cortical neurite loss to functional impairment after stroke and other conditions in which the innate immune response is activated.

The teleological role of CAR formation in mature neurites remains uncertain, but evidence suggests that, over short time intervals, rod formation conserves local energy ATP levels by blocking actin-dependent processes [15,16,18]. However, extensive or sustained CAR formation leads to neurite degeneration [7-10], as shown here. We additionally show that the brain inflammatory response is sufficient to induce this mechanism of neurite degeneration, and that interventions targeting either NOX2 activation or CAR formation can be effective in limiting inflammation-induced neurite degeneration.

Limitations of the study

Our results used an artificial stimulus that produced inflammation in the absence of primary neuronal injury to prove principle that neurites are particularly vulnerable to inflammation-induced degeneration. However, stimuli such as stroke and brain trauma induce inflammatory responses over a range of intensities that depend upon distance from the primary injury site, presence or absence of blood products, and other factors. This spectrum of inflammatory responses would thus be expected to cause areas of neuronal death in addition to areas of more selective neurite loss. Both neuronal cell loss and selective neurite loss can cause functional impairment, and the relative contribution of these processes to net functional impairment after injuries such as stroke or trauma remains to be determined.

We used $p47^{phox-/-}$ mice and cells cultured from these mice to assess the role of superoxide production in CAR formation and neurite loss, as NOX2 requires $p47^{phox}$ to form an active NOX2 complex. A limitation of this approach is that $p47^{phox}$ deficiency could have other effects that influence M/M response to inflammatory stimuli. Studies using pharmacological NOX2 inhibition would obviate this concern and at the same time test a potential therapeutic approach.

Our cell culture studies show that activation of NOX2 in cells other than neurons is sufficient for S100β-induced CAR formation, but do not establish whether this is microglial or astrocyte NOX2. Microglia and macrophages express NOX2 at far higher levels than astrocytes [48,49] but all three cell types may contribute to the process of CAR formation and neurite injury. Similarly, microglia and infiltrating macrophages contribute to the innate brain response in vivo but are not distinguished from one another by the Iba-1 labeling used here [3,38]. We thus cannot estimate the relative contributions of these different cell types to CAR formation and neurite loss.

Acknowledgments: This work was supported by the NIH (JRB-1R01AG044812) and by the Dept. of Veterans Affairs (RAS-1IO1 BX004884). These sponsors were not involved in study design, data analysis, decision to publish, or other aspects of this work. We thank Rebecca Fong and Jaqueline Davis for expert technical assistance.

Author contributions: Conceptualization: GU, RAS; Methodology: GU, AES, JRB, RAS; Investigation: GU, EM, AES, JRB, RAS; Visualization: GU, AES; Funding acquisition: JRB, RAS; Project administration: GU, EM, RAS; Supervision: JRB, RAS; Writing – original draft: GU, RAS; Writing – review & editing: GU, JRB, RAS.

Declaration of interests

The authors declared no potential conflicts of interest with respect to the research, authorship, and/or publication of this article.

Inclusion and diversity

We support inclusive, diverse, and equitable conduct of research.

STAR★Methods

Key Resources Table

REAGENT or RESOURCE	SOURCE	IDENTIFIER
Antibodies		
Affinity purified Rabbit anti-cofilin-1	Cell Signaling Technologies	Cat# 51755, RRID: AB_10622000
Rabbit pan ADF/cofilin antibody #1439	Prof. James Bamburg, Colorado State University	N/A
Mouse anti-Cofilin-1 antibody mAb22	Prof. James Bamburg, Colorado State University	N/A
Mouse anti-Neurofilament H (NF-H/SMI31)	Biolegend	Cat# 801601, RRID: AB_2564641
Mouse anti-Microtubule associated protein (MAP-2)	Millipore-Sigma	Cat# MAB3418, RRID: AB_11212326
Biotin tagged Mouse anti-Neuronal Nuclei (NeuN)	Millipore-Sigma	Cat# MAB377B, RRID: AB_177621
Rabbit Anti-Iba1	Wako	Cat# 019-19741, RRID: AB_839504
Mouse anti-GAPDH	Millipore-Sigma	Cat# mAb374, RRID: AB_2107445
Streptavidin, DyLight 405	Jackson Immunoresearch	Cat# 016-470-084, RRID: AB_2337248
Donkey Anti-Mouse, Alexa Fluor 488	Life technologies	Cat# A21202, RRID: AB_141607
Donkey Anti-Rabbit, Alexa Fluor 594	Invitrogen	Cat# A21207, RRID: AB_141637
Donkey anti-mouse IgG Fab fragments	Jackson Immunoresearch	Cat# 715-007-003, RRID: AB_2307338
Goat Anti-Mouse, DyLight 680	ThermoFisher	Cat# PI35518, RRID: AB_614942
Goat Anti-Rabbit, DyLight 800	ThermoFisher	Cat# PISA510036, RRID: AB_2556774
Chemicals, peptides, and recombinant proteins		
DMEM, no glucose, no glutamine, no phenol red	ThermoFisher	Cat# A1443001
Fetal Bovine Serum (FBS)	ThermoFisher	Cat# A5670501
Glucose	ThermoFisher	Cat# A2494001
Pyruvate	ThermoFisher	Cat# 11360070

L-glutamine	ThermoFisher	Cat# A2916801
Penicillin- Streptomycin	ThermoFisher	Cat# 15070063
Trypsin-EDTA	ThermoFisher	Cat# 25200072
Poly-D-lysine	ThermoFisher	Cat# A3890401
Neurobasal™-A Medium, no D-glucose, no sodium pyruvate	ThermoFisher	Cat# A2477501
Glutamax	ThermoFisher	Cat# 35050061
B27 supplement	ThermoFisher	Cat# 0080085SA
Recombinant mouse S100β	Novus Biologicals	Cat# NBP2-53070
Lipopolysaccharide (LPS)	Millipore-Sigma	Cat# L2630
Propidium Iodide	ThermoFisher	Cat# P1304MP
Nitrocellulose membrane	ThermoFisher	Cat# 45-004-010
Experimental models: Organisms/strains		
C57Bl/6 wild-type (WT) mice	Jackson Laboratories	Strain: #:000664 RRID: IMSR_JAX:000664
Thy1-YFP mice	Jackson Laboratories	Strain #:003709 RRID: IMSR_JAX:003709
Cofilin hemizygous ($COF^{-/+}$) mice	Prof. James Bamburg, Colorado State University	N/A
$p47^{phox-/-}$ mice	Jackson Laboratories	Strain #:027331 RRID: IMSR_JAX:027331
Software and algorithms		
ImageJ/Fiji	NIH	https://imagej.net/software/fiji/
Prism- GraphPad	Dotmatics	https://www.graphpad.com/scientific-software/prism/www.graphpad.com/scientific-software/prism/
Endnote 20	Clarivate	https://endnote.com/?language=en
Adobe Photoshop	Adobe	https://www.adobe.com/products/photoshop.html/
Adobe Illustrator	Adobe	https://www.adobe.com/products/illustrator.html/

Resource availability

Lead contact

Further information and requests for resources and reagents should be directed to and will be fulfilled by the lead contact, Raymond Swanson (raymond.swanson@ucsf.edu).

Materials availability

This study reports a novel mouse line, cofilin hemizygous ($COF^{-/+}$) mice. These mice will be made available upon request to the lead author.

Data And Code Availability

- All aggregated data are available in the main text and figures or the supplementary materials. Primary data (e.g. images and spreadsheets) will be provided upon written request to the lead contact.
- This paper does not report any original code.
- Any additional information can be requested directly from the lead contact.

Experimental model and subject details

Mice

Studies were approved by the Institutional Animal Care and Use Committees at the San Francisco Veterans Affairs Medical Center and Colorado State University and were performed in accordance with the National Institutes of Health Guide for the Care and Use of Laboratory Animals. Results are reported in accordance with the ARRIVE guidelines. C57Bl/6 wild-type, Thy1-YFP, and $p47^{phox-/-}$ mice were obtained from Jackson Laboratories. The $p47^{phox-/-}$ colony has been maintained as homozygotes and backcrossed to C57Bl/6 wild-type mice every 10 generations. Cofilin hemizygous ($COF^{-/+}$) mice were generated as described in Suppl. Fig. 4, and subsequently back-crossed > 8 generations to C57Bl/6 mice.

Cell culture preparations

Glial cultures, containing astrocytes and microglia, were prepared from postnatal day 0 or 1 C57BL/6 WT and $p47^{phox-/-}$ mice of both sexes as described [50]. The dissociated cells were plated and maintained in a 37°C, 5% CO_2 incubator in DMEM (ThermoFisher) containing 10% fetal bovine serum (FBS), 5 mM glucose, 1 mM pyruvate, 2 mM L-glutamine, 100U / ml penicillin, and 100 µg / ml streptomycin. At confluency, the cells were lifted by trypsin-EDTA and re-plated onto poly-D-lysine - coated coverslips at a density of 2×10^5 cells / 12 mm coverslip. Neurons from WT or

cofilin-1 hemizygous ($COF^{-/+}$) mice were isolated from embryonic day 16 mice as described [51] and plated directly onto the glial cultures. The co-cultures were then maintained in Neurobasal A medium (Thermo-Fisher, #21103049), containing 5 mM glucose, 0.2 mM pyruvate 1 mM Glutamax (ThermoFisher), and B27 supplement (ThermoFisher) in a 5% CO_2, 37° C incubator.

Method Details

Western blotting and characterization of cofilin-1 hemizygous mice

The hindbrains of embryonic (E10.5) mouse pups were quickly frozen in liquid nitrogen. Protein was solubilized by probe sonication into 100 µl Laemmli sample buffer, boiled for 3 minutes, run on a 15% SDS-PAGE gel, then transferred to nitrocellulose. Blots were blocked with bovine serum albumin, then incubated with previously characterized primary antibodies, detected on an Odyssey Infrared scanner and quantified with normalization to GAPDH. Two dimensional western blots were performed as described [21,52]. After transfer to nitrocellulose and blocking, cofilin and its phosphorylated form were immunolabelled with rabbit pan ADF/cofilin antibody [21,53].

Intracortical injections

All studies used equal numbers of male and female mice, age 3 - 4 months. Stereotaxic intracortical injections of lipopolysaccharide (LPS; Millipore), recombinant mouse S100β (Novus Biologicals) or saline (vehicle) were performed under 1.5 % isoflurane anesthesia. Injections were made into the right primary motor cortex (AP 1.0, ML 2.0, DV 1.0 mm from Bregma) in 0.5 µl volumes at 0.2 µl / minute. In some studies, the S100β was denatured by heating to 95° C for 60 minutes.

Motor function testing

Mice were placed at the center of the corner apparatus consisting of two adjacent walls that form a 30-degree angle [54]. The direction the mouse turned when it reached the corner was recorded over 10 trials on each day of testing. Data are presented as the percentage of turns made to the left.

Histology

Anesthetized mice were perfused with ice-cold saline followed by a solution of 4% paraformaldehyde in phosphate-buffered saline (PFA). Brains were removed and post-fixed in 4% PFA for 24 hours, then immersed for another 24 hours in 20% sucrose for cryoprotection, frozen, and cut into 40 µm coronal sections with a cryostat. The sections were permeabilized with 95% methanol and 5% 0.1 M phosphate buffer (PB) at -20° C for 15 minutes, then incubated with 10 mM sodium citrate (pH: 6.0) at 80° C for 30 minutes. The sections were incubated with unconjugated donkey anti-mouse IgG Fab fragments (Jackson Immunoresearch), diluted 1:35 in 0.1 M PB overnight at 4° C. On the following day the sections were incubated in blocking buffer (2% donkey serum and 0.1% bovine serum albumin (BSA) in 0.1 M PB) for one hour, and then incubated with

primary antibody overnight at 4° C. After washing, the sections were incubated with secondary antibodies for one hour or, where labeling was additionally performed with biotin-tagged primary antibodies, the sections were incubated with fluorescently tagged streptavidin (Jackson Immunoresearch, 1:250 in 0.1 M PB). Stained sections were mounted on glass slides in antifade mounting medium (Vector laboratories). Control sections omitting either primary or secondary antibodies showed no signal above background.

Primary antibodies were obtained from the following sources and used at 1:500 dilutions: rabbit anti-cofilin-1, Cytoskeleton #ACFL02, Denver, CO; mouse anti-MAP-2, Millipore #3418, Temecula, CA; mouse anti-NeuN, Millipore #MAB377B, Temecula, CA; mouse anti-NF-H, BioLegend #SMI31, San Diego, CA; rabbit anti- Phospho-Histone H2AX (Ser139) Antibody #2577; rabbit Iba1, Wako 019-19741. Secondary antibodies were obtained from the following sources and used at designated dilutions: Alexa Fluor 488 Donkey Anti-Mouse IgG (H+L) (1:500, Invitrogen # A-21202), Alexa Fluor 594 Donkey Anti-Rabbit IgG (H+L) (1:500, Invitrogen #A-11058), Alexa Fluor 405 Goat Anti-Mouse IgG (H+L) (1:250, Invitrogen # A-31553), Alexa Fluor 488 Goat Anti-Rabbit IgG (H+L) (1:500, Invitrogen # A-11008), DyLight 405 Streptavidin (1:250, Jackson Immunoresearch #016-470-084).

Cell culture studies

Studies were initiated by exchanging medium to fresh medium omitting the B27 supplement. Recombinant mouse S100β or LPS were added from concentrated stocks. Immunostaining of cell cultures was performed as described for brain sections but without the incubations in sodium citrate or donkey anti-mouse IgG Fab fragments. Where used to assess cell viability, propidium Iodide was added to the cultures 10 minutes before fixation.

Image analysis

All photographs were prepared with the same microscope under identical illumination and data capture conditions. Both the persons taking the photographs and analyzing the immunostaining were blinded to the treatment conditions. For cell culture studies, images were taken from five arbitrary regions of each cell culture well. For brain sections, confocal images were taken at four pre-determined locations 0.5 mm to the injection site on two sections from each animal. The confocal images were z-stacked, and each processed image was prepared using a stack of 10 1-μm thick Z- stage images. For assessments of CAR formation, images were thresholded using the Triangle function in ImageJ. The area of CAR signal was measured and normalized in two ways. First, it was expressed as percent of the NF-H area plus cofilactin area (for WT mice) or MAP-2 area plus cofilactin area (for cell cultures), because MAP2 and NF-H signals are lost where CARs form. As a second approach, the CAR area measurements were normalized to neuronal number. In each case, the CAR values obtained in each brain section image were averaged to provide an aggregate value for each brain, and values in the culture wells were averaged to provide an aggregate value

for each independent cell culture experiment. Neurite area measurements were made after thresholding the NF-H or MAP-2 images using the ImageJ Otsu or Li functions, respectively. Total YFP-expressing or NF-H-stained neurite length for each image was quantified by summing the length of neurites after skeletonizing the images in ImageJ. The neurite area and neurite length measurements in each image were normalized to the number of neuronal cell bodies in the image, as assessed by YFP (+) soma or NeuN immunostaining.

Microglia/macrophage responses to S100β or LPS were assessed by 3 methods [37]. The total number of Iba1+ cells was assessed using ImageJ/Fiji macro. Activated Iba1+ cells were manually labeled based on the previously published parameters [37]. Iba1+ microglial extension area was quantified after excluding the cell body areas on ImageJ using the particle size function. γH2AX staining intensity was measured in neuronal nuclei of cell cultures as defined by NeuN. Neurons were designated as "γH2AX-positive" when the integrated nuclear γH2AX density exceeded the 80th percentile of values measured in the corresponding control images for that experiment. Thus, by definition, 20% of neurons were γH2AX-positive in all control wells.

Quantification and statistical analysis

The "n" of each study defined as the number of mice or, for cell cultures, the number of independent experiments. Each independent experiment contained triplicate or quadruplicate culture wells. Numerical data were expressed as means ± SEM and analyzed using one-way ANOVA by either the Tukey–Kramer test where multiple groups were compared against one another, or Dunnett's test where multiple groups were compared against a common control group. Where only two groups were compared, the two-sided t-test was used. All data analysis was performed by individuals who were blinded to the experimental conditions.

References and Notes

1. Chen, Y., Won, S.J., Xu, Y., and Swanson, R.A. (2014). Targeting Microglial Activation in Stroke Therapy: Pharmacological Tools and Gender Effects. Curr Med Chem *21*, 2146-2155. CMC-EPUB-58355 [pii].
2. Salter, M.W., and Stevens, B. (2017). Microglia emerge as central players in brain disease. Nat Med *23*, 1018-1027. 10.1038/nm.4397.
3. Faraco, G., Sugiyama, Y., Lane, D., Garcia-Bonilla, L., Chang, H., Santisteban, M.M., Racchumi, G., Murphy, M., Van Rooijen, N., Anrather, J., and Iadecola, C. (2016). Perivascular macrophages mediate the neurovascular and cognitive dysfunction associated with hypertension. J Clin Invest *126*, 4674-4689. 10.1172/JCI86950.
4. Brown, G.C., and Neher, J.J. (2010). Inflammatory neurodegeneration and mechanisms of microglial killing of neurons. Mol Neurobiol *41*, 242-247. 10.1007/s12035-010-8105-9.
5. Shields, D.C., Haque, A., and Banik, N.L. (2020). Neuroinflammatory responses of microglia in central nervous system trauma. J Cereb Blood Flow Metab *40*, S25-S33. 10.1177/0271678X20965786.
6. Bartels, T., De Schepper, S., and Hong, S. (2020). Microglia modulate neurodegeneration in Alzheimer's and Parkinson's diseases. Science *370*, 66-69. 10.1126/science.abb8587.
7. McGough, A., Pope, B., Chiu, W., and Weeds, A. (1997). Cofilin changes the twist of F-actin: implications for actin filament dynamics and cellular function. J Cell Biol *138*, 771-781. 10.1083/jcb.138.4.771.
8. Galkin, V.E., Orlova, A., Kudryashov, D.S., Solodukhin, A., Reisler, E., Schroder, G.F., and Egelman, E.H. (2011). Remodeling of actin filaments by ADF/cofilin proteins. Proc Natl Acad Sci U S A *108*, 20568-20572. 10.1073/pnas.1110109108.
9. Hayden, S.M., Miller, P.S., Brauweiler, A., and Bamburg, J.R. (1993). Analysis of the interactions of actin depolymerizing factor with G- and F-actin. Biochemistry *32*, 9994-10004. 10.1021/bi00089a015.
10. Rahman, T., Davies, D.S., Tannenberg, R.K., Fok, S., Shepherd, C., Dodd, P.R., Cullen, K.M., and Goldsbury, C. (2014). Cofilin rods and aggregates concur with tau pathology and the development of Alzheimer's disease. Journal of Alzheimer's disease : JAD *42*, 1443-1460. 10.3233/JAD-140393.
11. Bamburg, J.R., Minamide, L.S., Wiggan, O., Tahtamouni, L.H., and Kuhn, T.B. (2021). Cofilin and Actin Dynamics: Multiple Modes of Regulation and Their Impacts in Neuronal Development and Degeneration. Cells *10*. 10.3390/cells10102726.
12. Hylton, R.K., Heebner, J.E., Grillo, M.A., and Swulius, M.T. (2022). Cofilactin filaments regulate filopodial structure and dynamics in neuronal growth cones. Nat Commun *13*, 2439. 10.1038/s41467-022-30116-x.
13. Kanellos, G., and Frame, M.C. (2016). Cellular functions of the ADF/cofilin family at a glance. J Cell Sci *129*, 3211-3218. 10.1242/jcs.187849.

14. Bernstein, B.W., Shaw, A.E., Minamide, L.S., Pak, C.W., and Bamburg, J.R. (2012). Incorporation of cofilin into rods depends on disulfide intermolecular bonds: implications for actin regulation and neurodegenerative disease. J Neurosci *32*, 6670-6681. 10.1523/jneurosci.6020-11.2012.
15. Bernstein, B.W., and Bamburg, J.R. (2010). ADF/cofilin: a functional node in cell biology. Trends Cell Biol *20*, 187-195. 10.1016/j.tcb.2010.01.001.
16. Bernstein, B.W., Chen, H., Boyle, J.A., and Bamburg, J.R. (2006). Formation of actin-ADF/cofilin rods transiently retards decline of mitochondrial potential and ATP in stressed neurons. Am J Physiol Cell Physiol *291*, C828-839. 10.1152/ajpcell.00066.2006.
17. Cichon, J., Sun, C., Chen, B., Jiang, M., Chen, X.A., Sun, Y., Wang, Y., and Chen, G. (2012). Cofilin aggregation blocks intracellular trafficking and induces synaptic loss in hippocampal neurons. J Biol Chem *287*, 3919-3929. 10.1074/jbc.M111.301911.
18. Bamburg, J.R., and Bernstein, B.W. (2016). Actin dynamics and cofilin-actin rods in alzheimer disease. Cytoskeleton (Hoboken) *73*, 477-497. 10.1002/cm.21282.
19. Bamburg, J.R., Bernstein, B.W., Davis, R.C., Flynn, K.C., Goldsbury, C., Jensen, J.R., Maloney, M.T., Marsden, I.T., Minamide, L.S., Pak, C.W., et al. (2010). ADF/Cofilin-actin rods in neurodegenerative diseases. Curr Alzheimer Res *7*, 241-250.
20. Minamide, L.S., Maiti, S., Boyle, J.A., Davis, R.C., Coppinger, J.A., Bao, Y., Huang, T.Y., Yates, J., Bokoch, G.M., and Bamburg, J.R. (2010). Isolation and characterization of cytoplasmic cofilin-actin rods. J Biol Chem *285*, 5450-5460. 10.1074/jbc.M109.063768.
21. Won, S.J., Minnella, A.M., Wu, L., Eun, C.H., Rome, E., Herson, P.S., Shaw, A.E., Bamburg, J.R., and Swanson, R.A. (2018). Cofilin-actin rod formation in neuronal processes after brain ischemia. PloS one *13*, e0198709. 10.1371/journal.pone.0198709.
22. Kim, J.S., Huang, T.Y., and Bokoch, G.M. (2009). Reactive oxygen species regulate a slingshot-cofilin activation pathway. Molecular biology of the cell *20*, 2650-2660. 10.1091/mbc.E09-02-0131.
23. Chao, C.C., Hu, S., Molitor, T.W., Shaskan, E.G., and Peterson, P.K. (1992). Activated microglia mediate neuronal cell injury via a nitric oxide mechanism. J Immunol *149*, 2736-2741.
24. Lavigne, M.C., Malech, H.L., Holland, S.M., and Leto, T.L. (2001). Genetic requirement of p47phox for superoxide production by murine microglia. FASEB J *15*, 285-287. 10.1096/fj.00-0608fje.
25. Bianchi, M.E. (2007). DAMPs, PAMPs and alarmins: all we need to know about danger. J Leukoc Biol *81*, 1-5. 10.1189/jlb.0306164.
26. Muhammad, S., Barakat, W., Stoyanov, S., Murikinati, S., Yang, H., Tracey, K.J., Bendszus, M., Rossetti, G., Nawroth, P.P., Bierhaus, A., and Schwaninger, M. (2008). The HMGB1 receptor RAGE mediates ischemic brain damage. J

Neurosci *28*, 12023-12031. 28/46/12023 [pii]10.1523/JNEUROSCI.2435-08.2008.
27. Donato, R., Cannon, B.R., Sorci, G., Riuzzi, F., Hsu, K., Weber, D.J., and Geczy, C.L. (2013). Functions of S100 proteins. Curr Mol Med *13*, 24-57.
28. Xu, J., Wang, H., Won, S.J., Basu, J., Kapfhamer, D., and Swanson, R.A. (2016). Microglial activation induced by the alarmin S100B is regulated by poly(ADP-ribose) polymerase-1. Glia *64*, 1869-1878. 10.1002/glia.23026.
29. Li, P., Stetler, R.A., Leak, R.K., Shi, Y., Li, Y., Yu, W., Bennett, M.V.L., and Chen, J. (2018). Oxidative stress and DNA damage after cerebral ischemia: Potential therapeutic targets to repair the genome and improve stroke recovery. Neuropharmacology *134*, 208-217. 10.1016/j.neuropharm.2017.11.011.
30. Chen, B., and Wang, Y. (2015). Cofilin rod formation in neurons impairs neuronal structure and function. CNS & neurological disorders drug targets *14*, 554-560.
31. Eidet, J.R., Pasovic, L., Maria, R., Jackson, C.J., and Utheim, T.P. (2014). Objective assessment of changes in nuclear morphology and cell distribution following induction of apoptosis. Diagn Pathol *9*, 92. 10.1186/1746-1596-9-92.
32. Cummings, B.S., and Schnellmann, R.G. (2004). Measurement of cell death in mammalian cells. Curr Protoc Pharmacol *Chapter 12*, Unit 12 18. 10.1002/0471141755.ph1208s25.
33. Woo, J.A., Zhao, X., Khan, H., Penn, C., Wang, X., Joly-Amado, A., Weeber, E., Morgan, D., and Kang, D.E. (2015). Slingshot-Cofilin activation mediates mitochondrial and synaptic dysfunction via Abeta ligation to beta1-integrin conformers. Cell Death Differ *22*, 921-934. 10.1038/cdd.2015.5.
34. Lyden, P.D., Bosetti, F., Diniz, M.A., Rogatko, A., Koenig, J.I., Lamb, J., Nagarkatti, K.A., Cabeen, R.P., Hess, D.C., Kamat, P.K., et al. (2022). The Stroke Preclinical Assessment Network: Rationale, Design, Feasibility, and Stage 1 Results. Stroke *53*, 1802-1812. 10.1161/STROKEAHA.121.038047.
35. Spiteri, A.G., Wishart, C.L., Pamphlett, R., Locatelli, G., and King, N.A.-O. Microglia and monocytes in inflammatory CNS disease: integrating phenotype and function.
36. Chen, W., Zhang, Y., Zhai, X., Xie, L., Guo, Y., Chen, C., Li, Y., Wang, F., Zhu, Z., Zheng, L., et al. Microglial phagocytosis and regulatory mechanisms after stroke.
37. Kauppinen, T.M., Suh Sw Fau - Berman, A.E., Berman Ae Fau - Hamby, A.M., Hamby Am Fau - Swanson, R.A., and Swanson, R.A. Inhibition of poly(ADP-ribose) polymerase suppresses inflammation and promotes recovery after ischemic injury.
38. Park, L., Uekawa, K., Garcia-Bonilla, L., Koizumi, K., Murphy, M., Pistik, R., Younkin, L., Younkin, S., Zhou, P., Carlson, G., et al. (2017). Brain Perivascular Macrophages Initiate the Neurovascular Dysfunction of Alzheimer Abeta Peptides. Circ Res *121*, 258-269. 10.1161/CIRCRESAHA.117.311054.
39. Berth, S.H., and Lloyd, T.E. (2023). Disruption of axonal transport in neurodegeneration. J Clin Invest *133*. 10.1172/JCI168554.

40. Niwa, R., Nagata-Ohashi, K., Takeichi, M., Mizuno, K., and Uemura, T. (2002). Control of actin reorganization by Slingshot, a family of phosphatases that dephosphorylate ADF/cofilin. Cell *108*, 233-246.
41. Walsh, K.P., Minamide, L.S., Kane, S.J., Shaw, A.E., Brown, D.R., Pulford, B., Zabel, M.D., Lambeth, J.D., Kuhn, T.B., and Bamburg, J.R. (2014). Amyloid-beta and proinflammatory cytokines utilize a prion protein-dependent pathway to activate NADPH oxidase and induce cofilin-actin rods in hippocampal neurons. PloS one *9*, e95995. 10.1371/journal.pone.0095995.
42. Brown, C.E., Li, P., Boyd, J.D., Delaney, K.R., and Murphy, T.H. (2007). Extensive turnover of dendritic spines and vascular remodeling in cortical tissues recovering from stroke. J Neurosci *27*, 4101-4109. 10.1523/JNEUROSCI.4295-06.2007.
43. Zhang, S., Boyd, J., Delaney, K., and Murphy, T.H. (2005). Rapid reversible changes in dendritic spine structure in vivo gated by the degree of ischemia. J Neurosci *25*, 5333-5338. 10.1523/JNEUROSCI.1085-05.2005.
44. Gao, X., Deng, P., Xu, Z.C., and Chen, J. (2011). Moderate traumatic brain injury causes acute dendritic and synaptic degeneration in the hippocampal dentate gyrus. PloS one *6*, e24566. 10.1371/journal.pone.0024566.
45. Rappert, A., Bechmann, I., Pivneva, T., Mahlo, J., Biber, K., Nolte, C., Kovac, A.D., Gerard, C., Boddeke, H.W., Nitsch, R., and Kettenmann, H. (2004). CXCR3-dependent microglial recruitment is essential for dendrite loss after brain lesion. J Neurosci *24*, 8500-8509. 10.1523/JNEUROSCI.2451-04.2004.
46. Moreno, B., Jukes, J.P., Vergara-Irigaray, N., Errea, O., Villoslada, P., Perry, V.H., and Newman, T.A. (2011). Systemic inflammation induces axon injury during brain inflammation. Ann Neurol *70*, 932-942. 10.1002/ana.22550.
47. Pang, D., Wu, Y.L., Alcamo, A.M., Cummings, J., Di Caro, V., Walko, T., 3rd, Hsue, V., Clark, R.S.B., Panigrahy, A., Kochanek, P.M., and Aneja, R.K. (2020). Early Axonal Injury and Delayed Cytotoxic Cerebral Edema are Associated with Microglial Activation in a Mouse Model of Sepsis. Shock *54*, 256-264. 10.1097/SHK.0000000000001446.
48. Ma, M.W., Wang, J., Zhang, Q., Wang, R., Dhandapani, K.M., Vadlamudi, R.K., and Brann, D.W. (2017). NADPH oxidase in brain injury and neurodegenerative disorders. Mol Neurodegener *12*, 7. 10.1186/s13024-017-0150-7.
49. Abramov, A.Y., Jacobson, J., Wientjes, F., Hothersall, J., Canevari, L., and Duchen, M.R. (2005). Expression and modulation of an NADPH oxidase in mammalian astrocytes. J Neurosci *25*, 9176-9184. 10.1523/JNEUROSCI.1632-05.2005.
50. Swanson, R.A., and Seid, L.L. (1998). Barbiturates impair astrocyte glutamate uptake. Glia *24*, 365-371. 10.1002/(sici)1098-1136(199812)24:4<365::aid-glia1>3.0.co;2-e.
51. Brennan, A.M., Suh, S.W., Won, S.J., Narasimhan, P., Kauppinen, T.M., Lee, H., Edling, Y., Chan, P.H., and Swanson, R.A. (2009). NADPH oxidase is the

primary source of superoxide induced by NMDA receptor activation. Nature neuroscience *12*, 857-863. 10.1038/nn.2334.

52. Shaw, A.E., Minamide, L.S., Bill, C.L., Funk, J.D., Maiti, S., and Bamburg, J.R. (2004). Cross-reactivity of antibodies to actin- depolymerizing factor/cofilin family proteins and identification of the major epitope recognized by a mammalian actin-depolymerizing factor/cofilin antibody. Electrophoresis *25*, 2611-2620. 10.1002/elps.200406017.
53. Abe, H., Ohshima, S., and Obinata, T. (1989). A cofilin-like protein is involved in the regulation of actin assembly in developing skeletal muscle. J Biochem *106*, 696-702. 10.1093/oxfordjournals.jbchem.a122919.
54. Zhang, L., Schallert, T., Zhang, Z.G., Jiang, Q., Arniego, P., Li, Q., Lu, M., and Chopp, M. (2002). A test for detecting long-term sensorimotor dysfunction in the mouse after focal cerebral ischemia. J Neurosci Methods *117*, 207-214. 10.1016/s0165-0270(02)00114-0.

FIGURE LEGENDS

Figure 1. **S100β induces neurite loss.** (**A, B**) Low- and high-magnification views of brain sections from Thy1-YFP mice harvested 3 days after S100β injection. Scale bar = 500 μm. In (A), the arrow shows the injection site, and the rectangle shows the area of higher-magnification views shown in panel B. In (B), neuronal cell nuclei are identified by NeuN immunostaining (magenta). Scale bar = 10 μm. (**C**). Quantification of neuronal cell body density. (**D, E**), YFP neurite length and area, expressed relative to saline-injected controls. n = 4, *p < 0.05, **p < 0.01, vs. saline controls by one-way ANOVA with Dunnett's test. All data are shown as mean ± SEM.

Figure 2. S100β induces cofilactin rod (CAR) formation and neurite loss.
(A) Diagram shows the locations of intracortical injections and peri-injection region imaged. **(B)** Cofilactin rod formation (CAR) identified by immunostaining for cofilin-1 aggregates (red) in WT mice after saline or 50 ng S100β injections. Neurites are identified by neurofilament-H (NF-H; green). Neurofilament H integrity is lost at sites of CAR formation. Scale bar = 10 μm. **(C-E)** CAR density expressed as percent of total neurite area. **(F)** Neurite loss 1, 3, and 7 days after saline or 50 ng S100β injections as assessed by immunostaining for NF-H (green), with neuronal cell nuclei identified by NeuN (magenta). Scale bar = 10 μm. **(G-I)** NF-H+ neurite length per neuronal nucleus in the S100β - injected mice. n = 4, **p < 0.01 by Student's t-test. All data are shown as mean ± SEM.

Figure 3. CAR formation is attenuated in both cofilin-1 hemizygous and p47^{phox} deficient mice.
(**A**) CAR formation after saline or 50 ng S100β injections in WT, COF$^{-/+}$ and p47$^{phox-/-}$ mice identified by immunostaining for cofilin-1 aggregates (red). Neurites are identified by neurofilament H (NF-H; green). Scale bar = 10 μm. (**B-D**) CAR density expressed as percent of total neurite area. **(E)** Neurite loss after saline or 50 ng S100β injections as assessed by immunostaining for NF-H (green), with neuronal cell nuclei identified by NeuN (magenta). Scale bar = 20 μm. **(F-H)** Neurite length per neuronal nucleus in the S100β injected mice relative to saline-injected mice of each genotype. n = 4; *p < 0.05, **p < 0.01 vs. WT mice by one-way ANOVA with Dunnett's test. All data are shown as mean ± SEM.

Figure 4. S100β-induced neurite loss and motor impairment are attenuated in cofilin-1 hemizygous and p47^{phox} deficient mice.
(**A**) Schematic timeline of behavioral assessments. (**B**) Performance on the corner test assessed by quantifying the percentage of left turns. n = 6 for each genotype. *p < 0.05, ** p < 0.01 vs. WT by one-way ANOVA with Dunnett's test. (**C**) Iba-1 immunostaining shows microglia/macrophage (M/M) activation 1 day after injection with 50 ng S100β. Inserts show magnified views. Responses to S100β injections were similar in the three mouse genotypes. Scale bars = 10 μm. (**D-F**) Quantification of M/M responses to

S100β. n = 4; *p < 0.05, **p < 0.01 vs. WT mice by one-way ANOVA with Dunnett's test. All data are shown as mean ± SEM.

Figure 5. **Lipopolysaccharide causes cofilactin rod formation and neurite loss.** **(A)** Photomicrographs from peri-injection cortex in WT mice at days 1 and 7 after injection of LPS (200 ng) or saline vehicle. Cofilactin rods are identified by cofilin-1 (red), neurites by neurofilament H (NF-H, green) and neuronal soma by NeuN (blue). Scale bar = 20 µm. **(B-C)** Cofilactin rod density expressed as percent of total neurite area. **(D-E)** Neuronal cell body density per mm^2. **(F-G)** Neurite length per neuronal nucleus. **(H-I)** Neurite area per neuronal nucleus. Neurite length and area determinations are expressed relative to saline controls. n = 4; *p < 0.05, **p < 0.01 by Student's test. All data are shown as mean ± SEM.

Figure 6. CAR formation in neuron-glia co-cultures is attenuated by both neuronal cofilin-1 hemizygosity and glial $p47^{phox}$ deficiency.
(**A**) Representative photomicrographs of co-cultures immunostained for microtubule-associated protein-2 (MAP-2) (blue) and cofilactin rods (CARs, green). Scale bar = 10 µm. (**B-D**) CAR density expressed as percent of total neurite area. n = 4; *p < 0.05, **p < 0.01 vs. control by one-way ANOVA with Dunnett's test. All data are shown as mean ± SEM.

Figure 7. Neurite loss in neuron-glia co-cultures is attenuated by neuronal cofilin-1 hemizygosity and glial $p47^{phox}$ deficiency.
(**A**) Photomicrographs of co-cultures immunostained for MAP-2 (green) and NeuN (blue). Scale bar = 20 µm. (**B-D**) Neurite length assessed at 4, 24, and 48 hours of 50 ng/ml S100β incubation, expressed relative to control wells of the respective co-culture type. n = 4; *p < 0.05, ** p < 0.01 by one-way ANOVA with Dunnett's test. (**E**) Mechanism proposed for inflammation-induced neurite degeneration. In response to pro-inflammatory stimuli, brain microglia and infiltrating macrophages upregulate superoxide production by NADPH oxidase. Resulting oxidative stress in nearby neurites leads to formation of cofilactin rods. Persistence of the cofilactin rods causes neurite degeneration, which can occur in the absence of parental neuron death. This process is attenuated in $p47^{phox-/-}$ mice, which cannot form an active NADPH oxidase-2 complex, and in cofilin hemizygous ($COF^{-/+}$) mice, which have reduced propensity to form cofilactin rods. All data are shown as mean ± SEM.

Figure 1

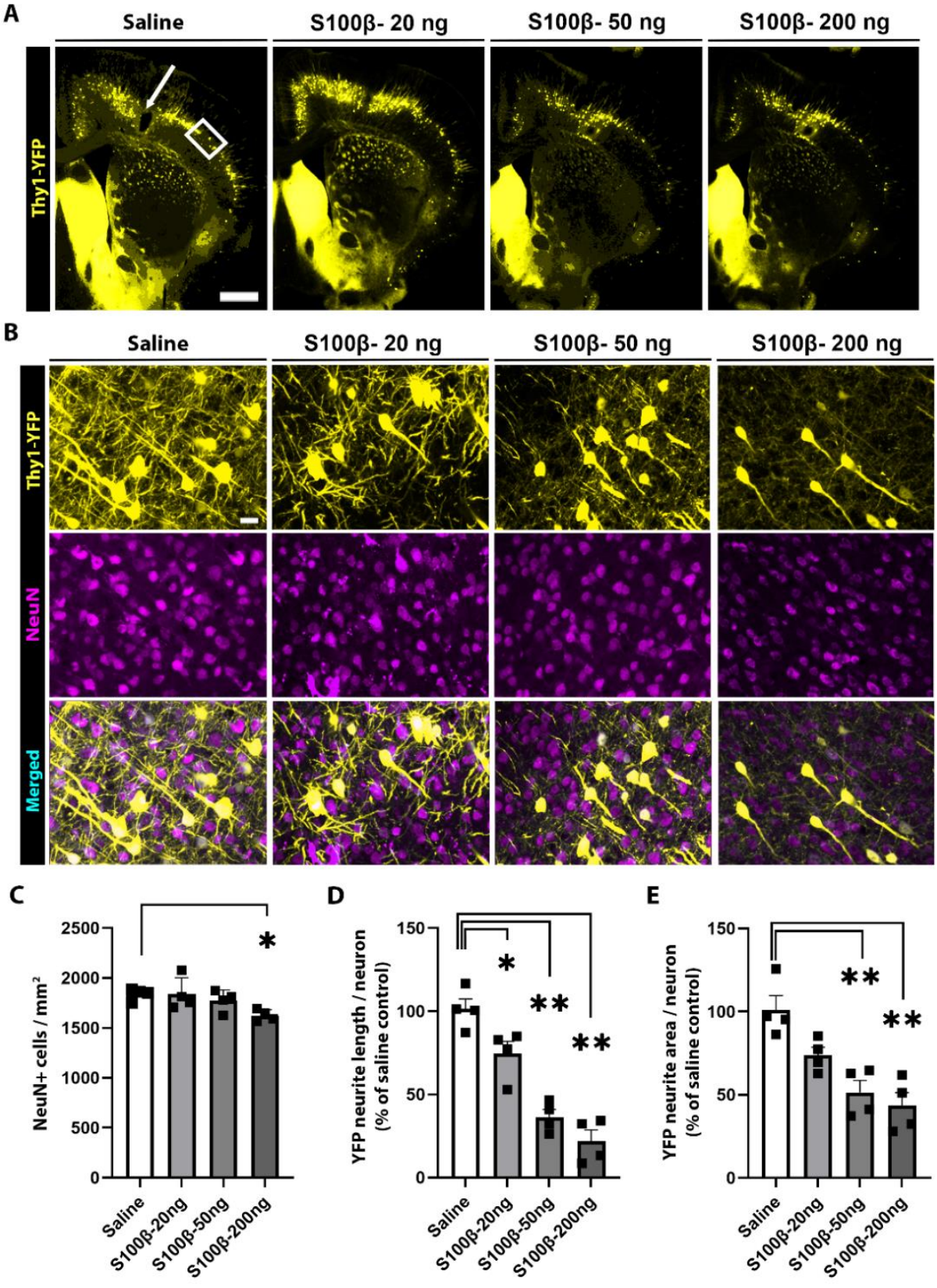
A
Saline
S100β- 20 ng
S100β- 50 ng
S100β- 200 ng
Thy1-YFP
B
Saline
S100β- 20 ng
S100β- 50 ng
S100β- 200 ng
Thy1-YFP
NeuN
Merged
C
NeuN+ cells / mm²
2500
2000
1500
1000
500
0
*
Saline
S100β-20ng
S100β-50ng
S100β-200ng
D
YFP neurite length / neuron (% of saline control)
150
100
50
0
*
**
**
Saline
S100β-20ng
S100β-50ng
S100β-200ng
E
YFP neurite area / neuron (% of saline control)
150
100
50
0
**
**
Saline
S100β-20ng
S100β-50ng
S100β-200ng

Figure 2

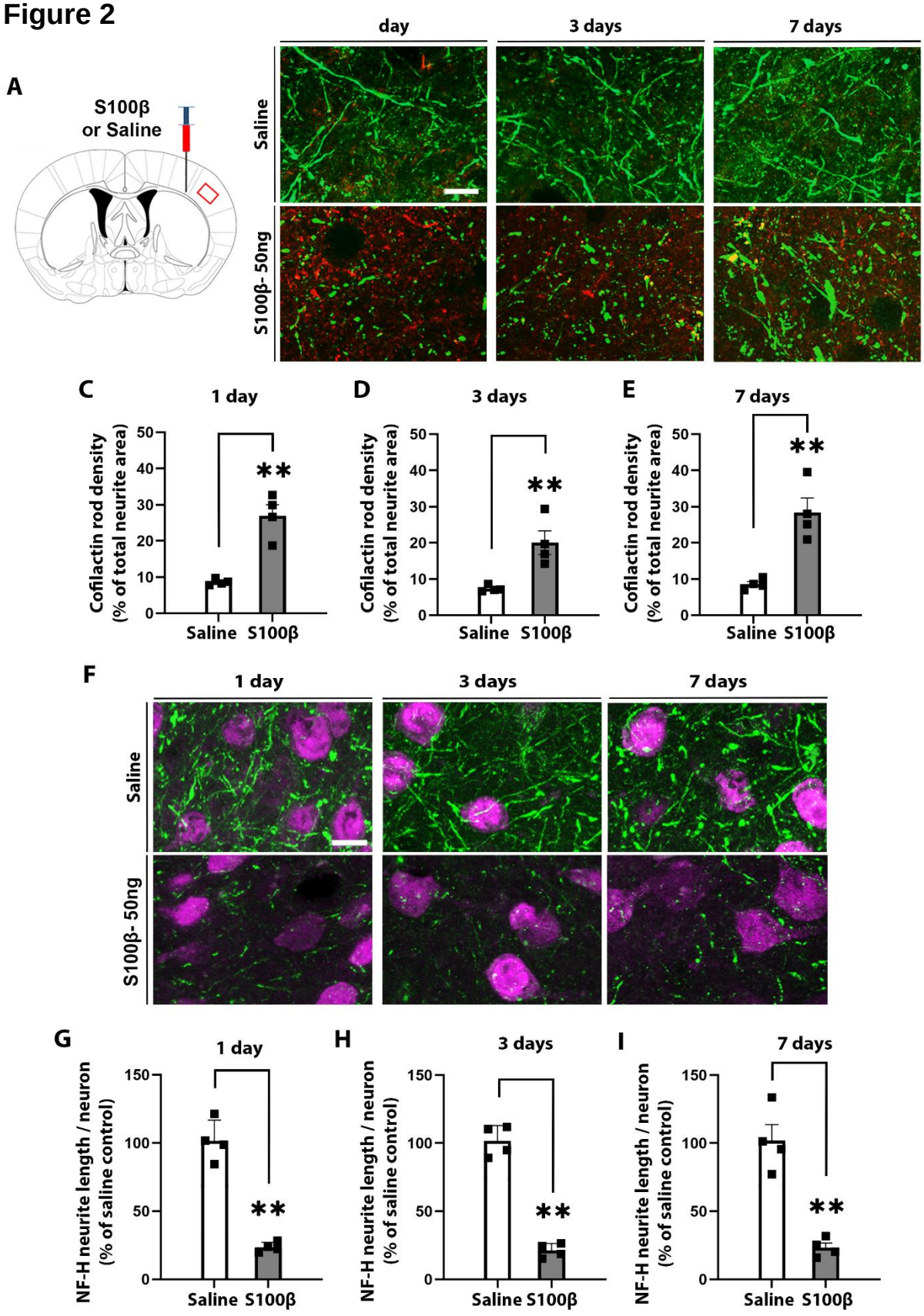
A
S100β
or Saline
day
3 days
7 days
Saline
S100β- 50ng
C
1 day
D
3 days
E
7 days
Cofilactin rod density
(% of total neurite area)
Saline
S100β
F
1 day
3 days
7 days
Saline
S100β- 50ng
G
1 day
H
3 days
I
7 days
NF-H neurite length / neuron
(% of saline control)
Saline
S100β

Figure 3

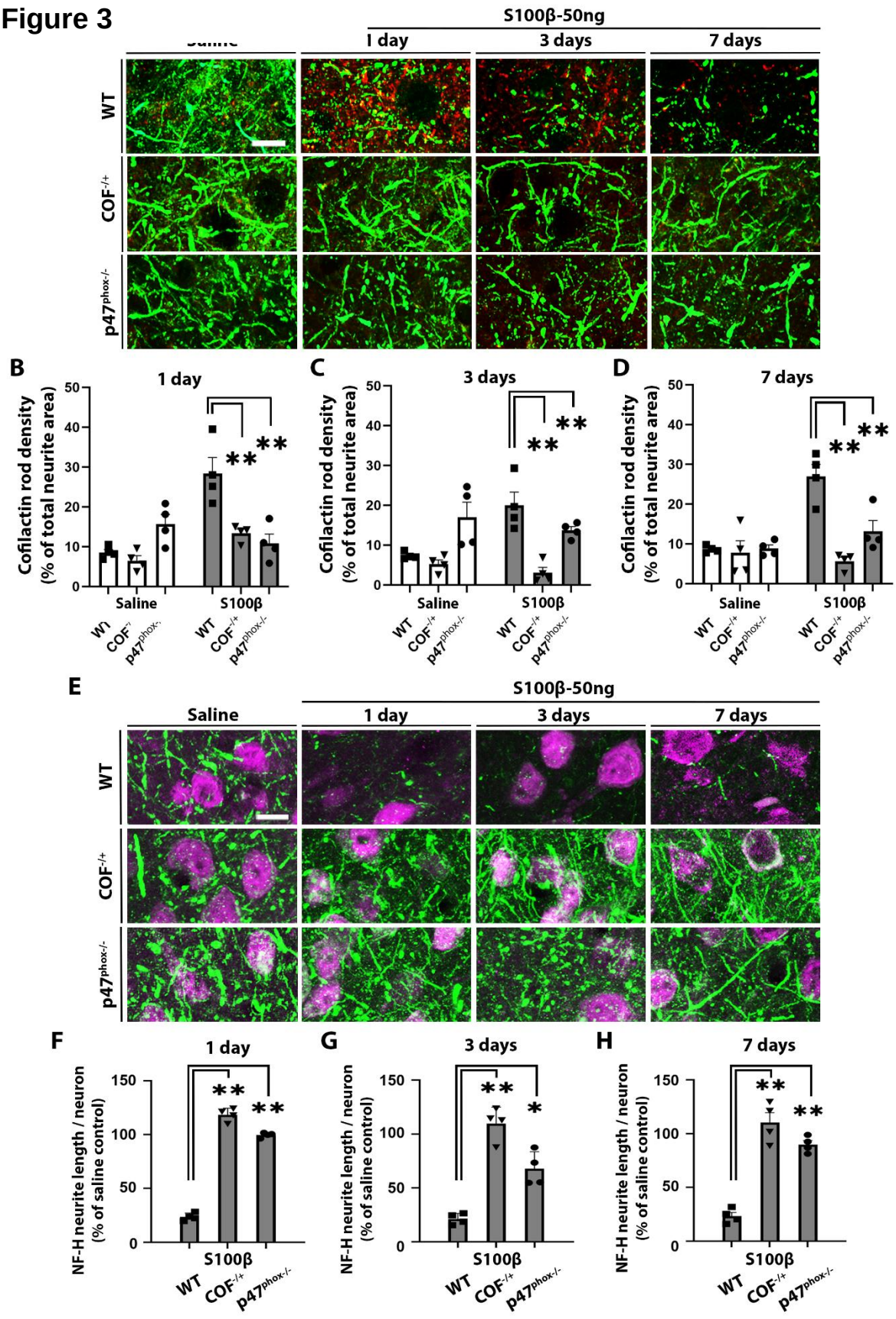
S100β-50ng
1 day
3 days
7 days
WT
COF-/+
p47phox-/-
B
1 day
C
3 days
D
7 days
Cofilactin rod density (% of total neurite area)
Saline
S100β
E
Saline
S100β-50ng
F
G
H
NF-H neurite length / neuron (% of saline control)

Figure 4

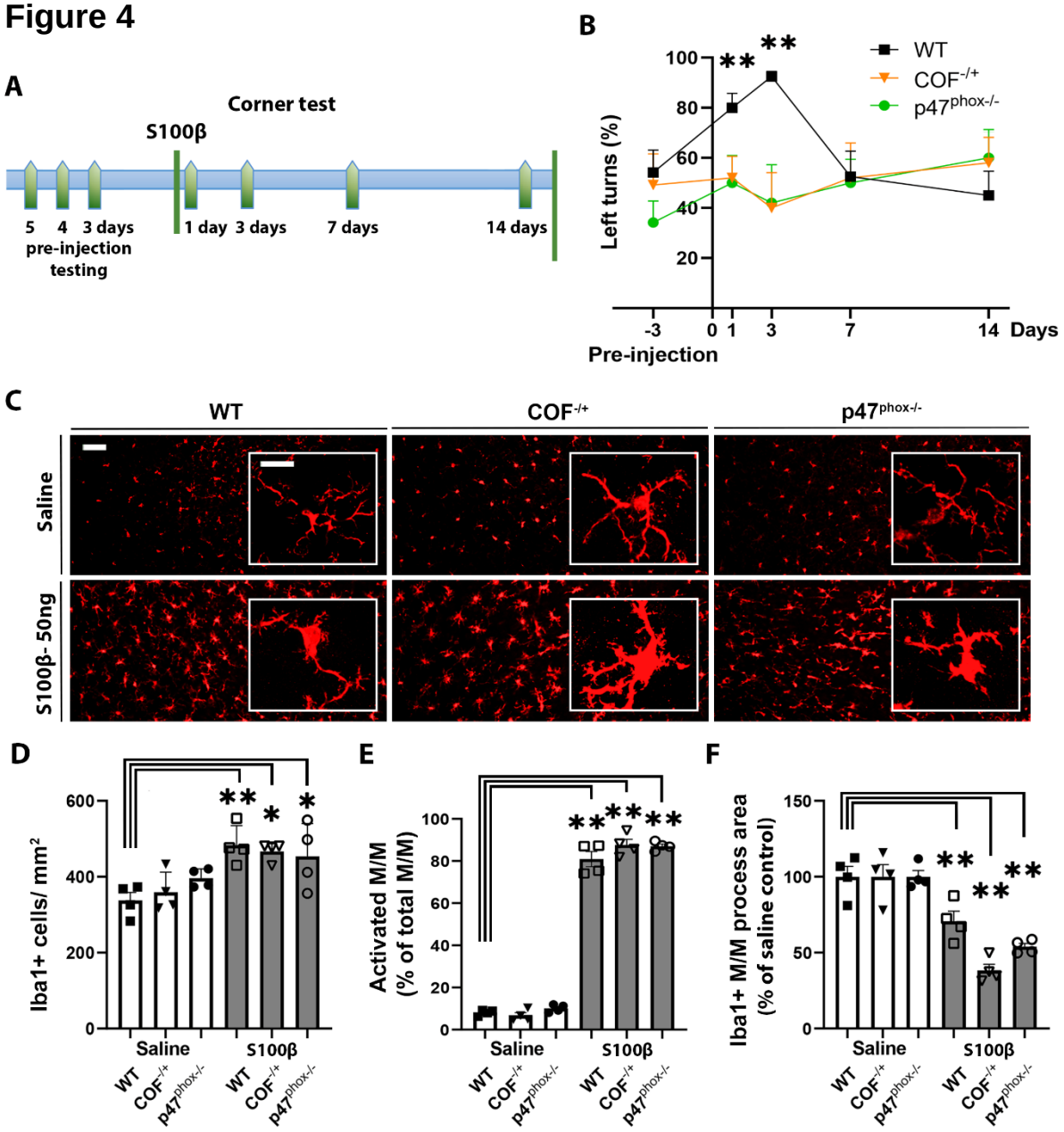
A
Corner test
S100β
5 4 3 days
pre-injection
testing
1 day 3 days
7 days
14 days
B
WT
COF-/+
p47phox-/-
Left turns (%)
Pre-injection
Days
C
WT
COF-/+
p47phox-/-
Saline
S100β- 50ng
D
Iba1+ cells/ mm2
E
Activated M/M
(% of total M/M)
F
Iba1+ M/M process area
(% of saline control)
Saline
S100β

Figure 5

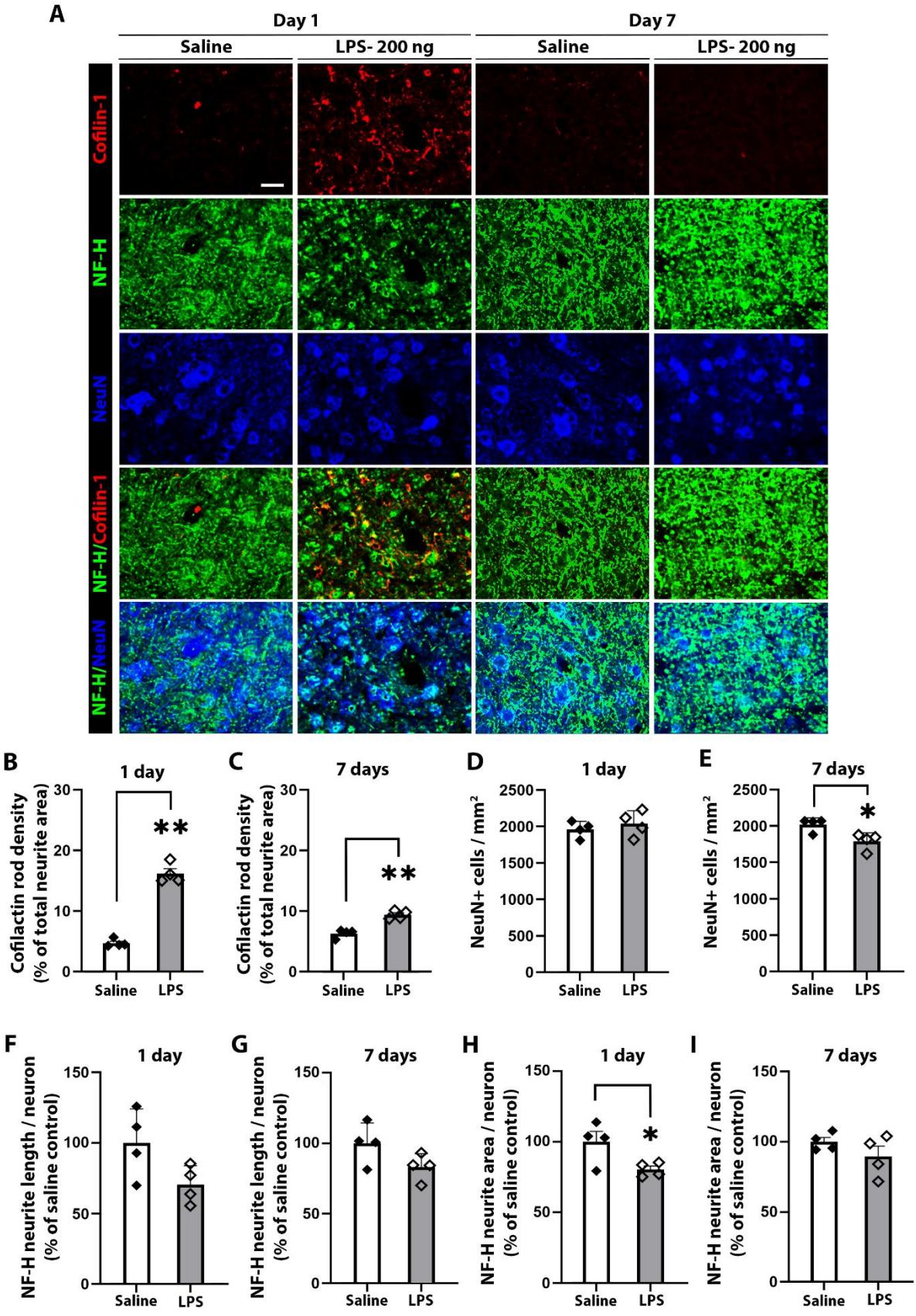
A
Day 1
Day 7
Saline
LPS- 200 ng
Saline
LPS- 200 ng
Cofilin-1
NF-H
NeuN
NF-H/Cofilin-1
NF-H/NeuN
B
1 day
Cofilactin rod density (% of total neurite area)
Saline
LPS
C
7 days
Cofilactin rod density (% of total neurite area)
Saline
LPS
D
1 day
NeuN+ cells / mm²
Saline
LPS
E
7 days
NeuN+ cells / mm²
Saline
LPS
F
1 day
NF-H neurite length / neuron (% of saline control)
Saline
LPS
G
7 days
NF-H neurite length / neuron (% of saline control)
Saline
LPS
H
1 day
NF-H neurite area / neuron (% of saline control)
Saline
LPS
I
7 days
NF-H neurite area / neuron (% of saline control)
Saline
LPS

Figure 6

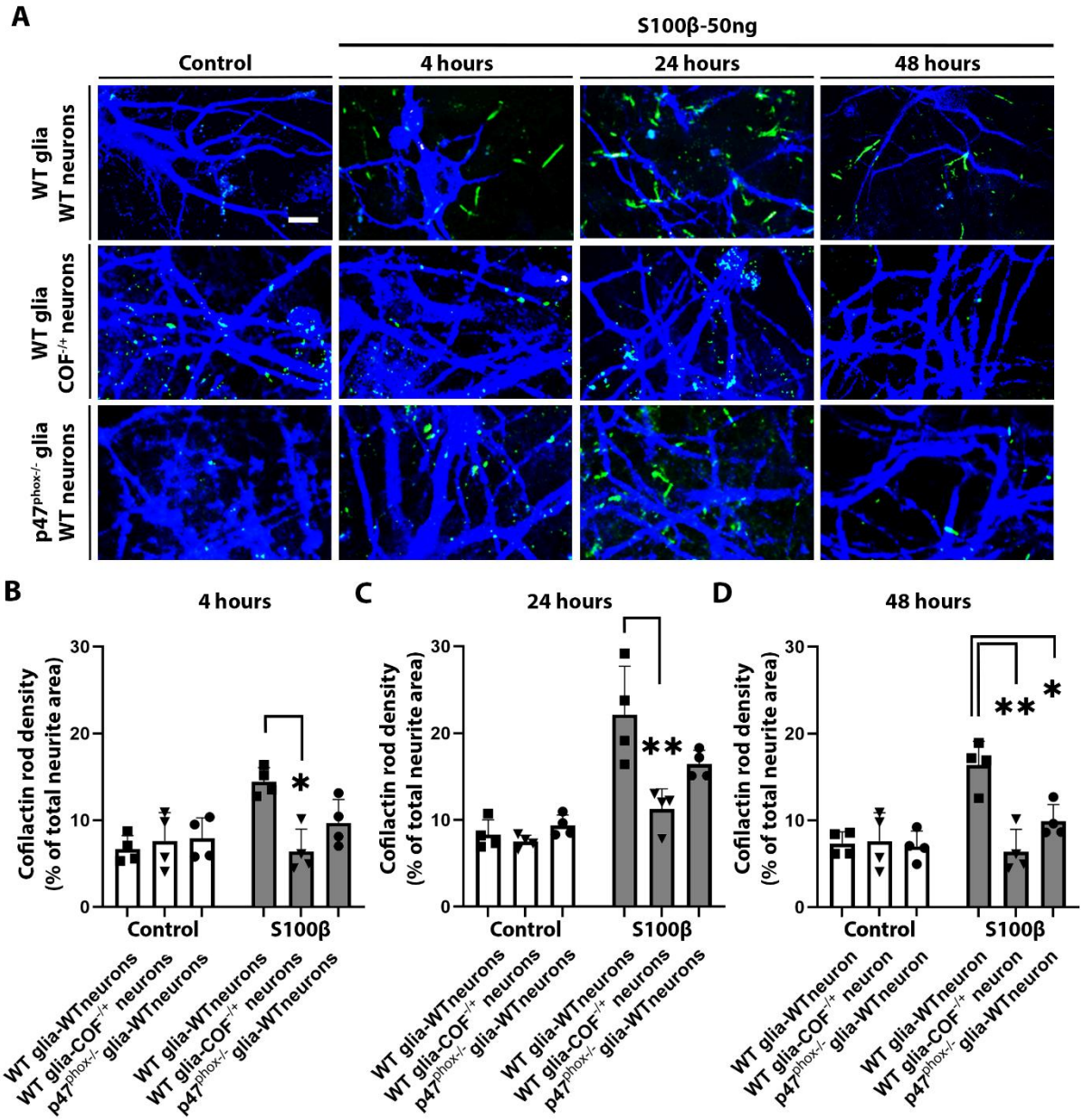
A
S100β-50ng
Control
4 hours
24 hours
48 hours
WT glia
WT neurons
WT glia
COF-/+ neurons
p47phox-/- glia
WT neurons
B
4 hours
C
24 hours
D
48 hours
Cofilactin rod density
(% of total neurite area)
Control
S100β
WT glia-WTneurons
WT glia-COF-/+ neurons
p47phox-/- glia-WTneurons
WT glia-WTneuron
WT glia-COF-/+ neuron
p47phox-/- glia-WTneuron

Figure 7

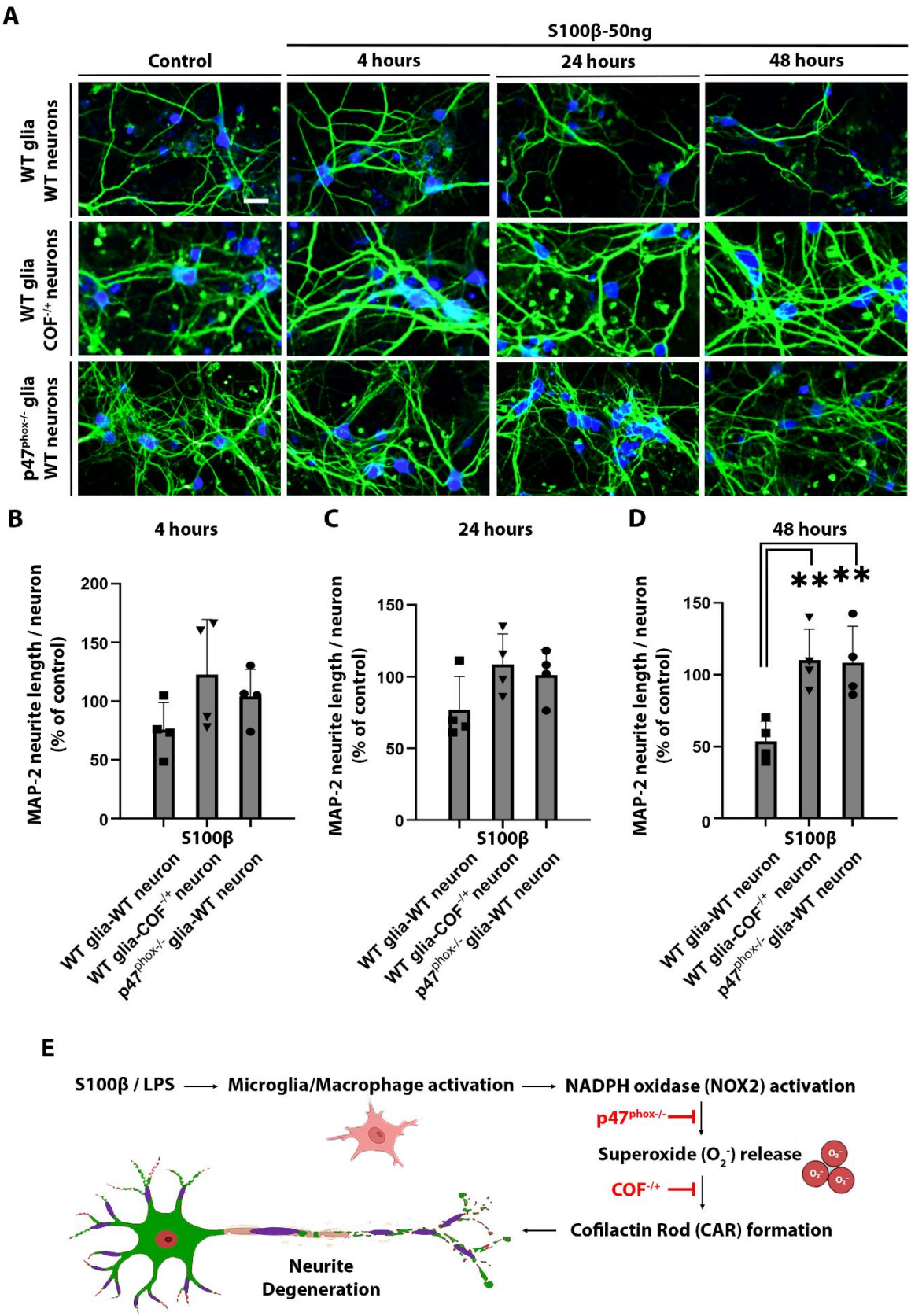
A
S100β-50ng
Control
4 hours
24 hours
48 hours
WT glia
WT neurons
WT glia
COF-/+ neurons
p47phox-/- glia
WT neurons
B
4 hours
C
24 hours
D
48 hours
****
MAP-2 neurite length / neuron
(% of control)
S100β
WT glia-WT neuron
WT glia-COF-/+ neuron
p47phox-/- glia-WT neuron
E
S100β / LPS
Microglia/Macrophage activation
NADPH oxidase (NOX2) activation
p47phox-/-
Superoxide (O2-) release
COF-/+
Cofilactin Rod (CAR) formation
Neurite
Degeneration

Cell Reports, Volume *43*

Supplemental information

Cofilactin rod formation mediates inflammation-induced neurite degeneration

Gökhan Uruk, Ebony Mocanu, Alisa E. Shaw, James R. Bamburg, and Raymond A. Swanson

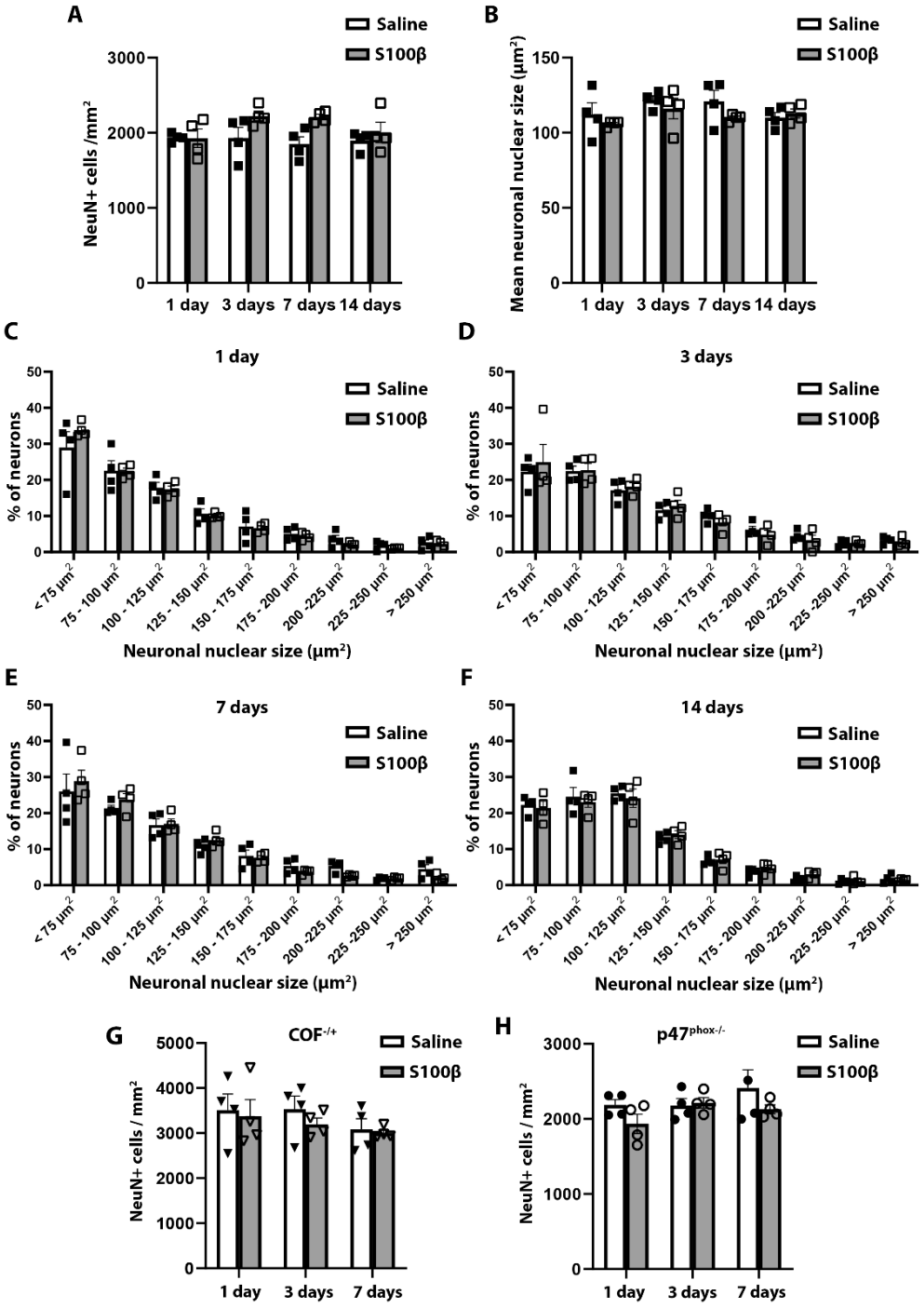

Figure S1, related to Figures 2 and 3. Neuronal loss as assessed by neuronal density and nuclear size.

(A, B) Quantification of neuronal cell body density and neuronal nuclear size at 1, 3, 7, and 14 days after 50 ng S100β injections in WT mice. (**C-F**) Histograms showing distribution of neuronal nuclei by size. (**G-H**) Quantification of neuronal cell body density in $COF^{-/+}$ and $p47^{phox-/-}$ mice after 50 ng S100β injections. n = 4; differences between saline and S100β not significant by ANOVA with Tukey tests between each pair of data. All data are shown as mean ± SEM.

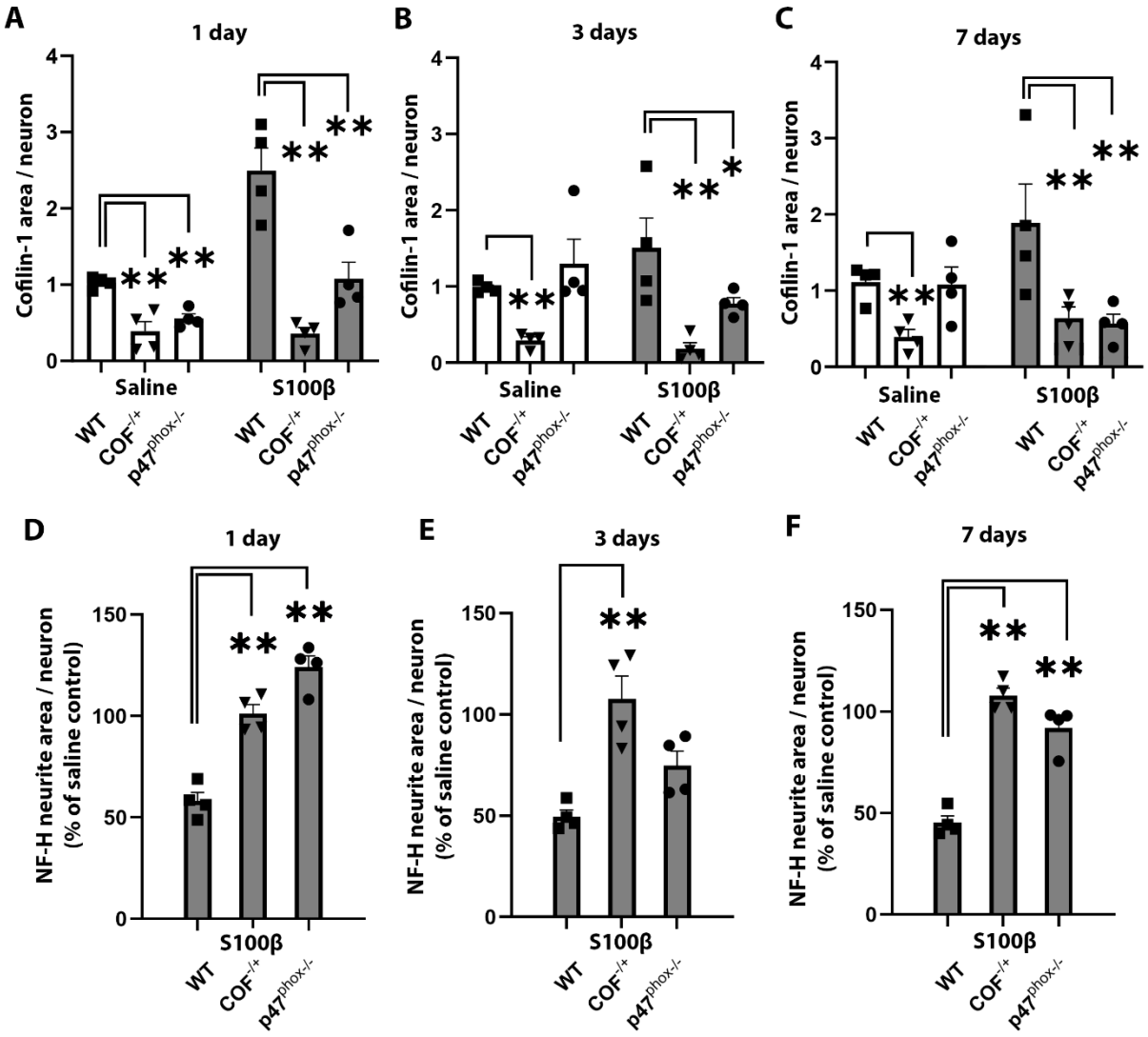

Figure S2, related to Figure 3. Cofilactin rod (CAR) formation and neurite loss as assessed by cofilactin and neurofilament-H area.

(A-C) Cofilactin rod area in mice of each genotype injected with saline or 50 ng S100β, normalized to neuron number. (Corresponding to the cofilactin rod / total neurite length assessments in Figure 3B-D). **(D-F)** NF-H+ neurite area in mice of each genotype injected with 50 ng S100β, normalized to neuron number and expressed relative to the corresponding saline-injected mice of each genotype (Corresponding to the neurite length assessments in Figure 3F-H). n = 4; *p < 0.05, **p < 0.01 by one-way ANOVA with Dunnett's test. All data are shown as mean ± SEM.

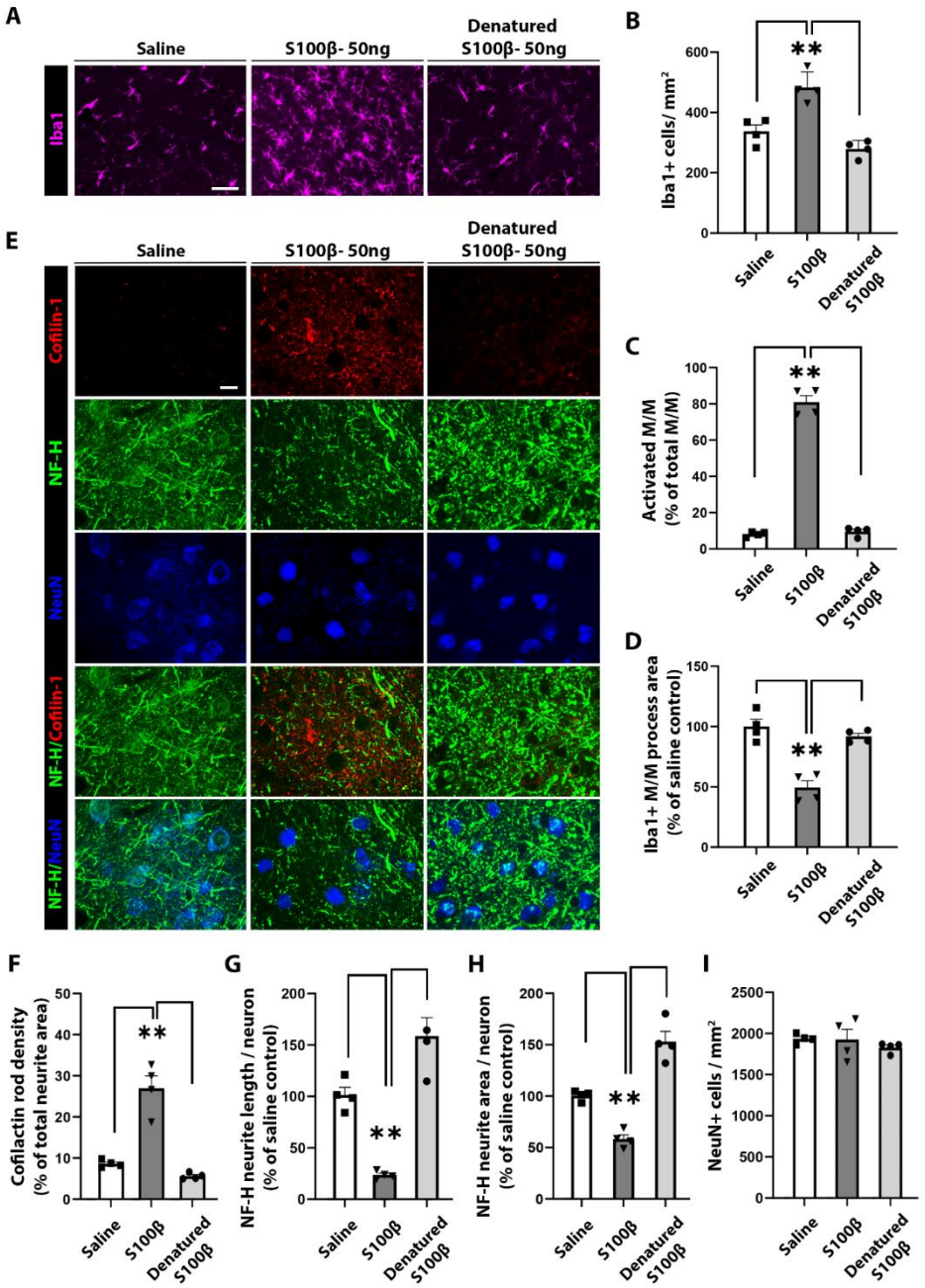

Figure S3, related to Figure 4. Denatured S100β does not induce microglia/macrophage activation, CAR formation, or neurite loss.

Photomicrographs from peri-injection cortex 1 day after injection of saline, 50ng S100β, or 50ng denatured S100β. **(A)** Microglia/macrophage (M/M) morphology by Iba1 immunostaining. Scale bar = 20 μm. **(B-D)** Quantification of M/M responses. **(E)** CAR formation identified by cofilin-1 (red) and neurites identified by neurofilament-H (NF-H), green), with neuronal nuclei identified by NeuN (blue). Scale bar = 20 μm. Graphs show quantification of CAR density **(G)**, NF-H length per neuronal nucleus **(H)**, NF-H-area per neuronal nucleus **(I)**, and neuronal cell density. The length and area determinations are expressed relative to saline controls prepared in parallel. n = 4; *p < 0.05, **p < 0.01 by one-way ANOVA with Dunnett's test. All data are shown as mean ± SEM.

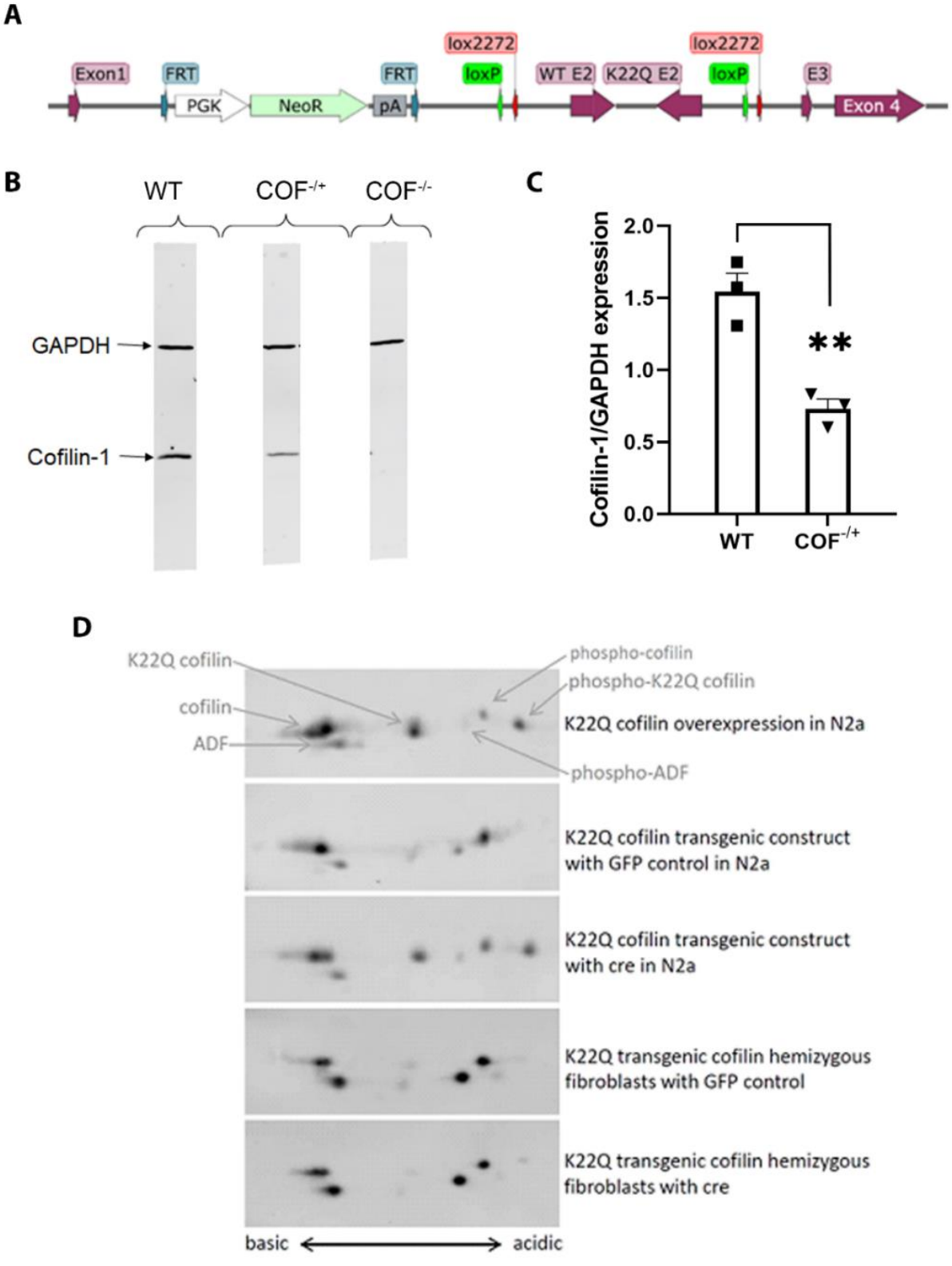
A
Exon1
FRT
PGK
NeoR
FRT
pA
lox2272
loxP
WT E2
K22Q E2
lox2272
loxP
E3
Exon 4
B
WT
COF-/+
COF-/-
GAPDH
Cofilin-1
C
Cofilin-1/GAPDH expression
2.0
1.5
1.0
0.5
0.0
**
WT
COF-/+
D
K22Q cofilin
cofilin
ADF
phospho-cofilin
phospho-K22Q cofilin
phospho-ADF
K22Q cofilin overexpression in N2a
K22Q cofilin transgenic construct with GFP control in N2a
K22Q cofilin transgenic construct with cre in N2a
K22Q transgenic cofilin hemizygous fibroblasts with GFP control
K22Q transgenic cofilin hemizygous fibroblasts with cre
basic
acidic

Figure S4, related to Figures 3 and 4. Generation of COF$^{-/+}$ mice.
The cofilin hemizygous mouse line used in this study was the result of an attempt to generate a conditional cofilin K22Q knock-in mouse that would not form cofilactin rods. The transgenic mouse was designed to have an inverted duplication of cofilin exon 2, in which wildtype cofilin would be expressed until irreversible inversion by cre recombinase to instead express a K22Q mutant cofilin that has reduced F-actin binding affinity and does not form CARs [S1]. The design of the transgenic targeting cassette is shown in panel **(A**) The presence of the transgenic allele in the resulting mouse line was confirmed by PCR and by DNA sequencing. Unexpectedly, the transgenic cofilin exon 2 was silent, expressing no wild-type or K22Q cofilin before or after cre inversion, resulting in a cofilin null allele. **(B, C)** Western blot gels and quantifications showed that the hemizygous K22Q cofilin mice express approximately half the wild-type amount of cofilin, and the homozygous mice are cofilin null. n = 4; *p < 0.05, **p < 0.01 by Student's t-test. Data are shown as mean ± SEM. **(D)** The lack of expression from the transgenic K22Q allele was further confirmed by expressing cre in hemizygous mouse dermal fibroblasts and detecting cofilin separated by 2D gel electrophoresis. Due to its altered pI, K22Q cofilin separates as distinct spots from wildtype cofilin during 2D gel electrophoresis, as shown by overexpression of K22Q cofilin in mouse N2a cell line, as well as by transfection of the K22Q cofilin transgenic targeting construct into N2a cells with or without cre co-expression. Primary dermal fibroblasts from hemizygous K22Q cofilin transgenic mouse pups were infected with adenovirus expressing either cre and GFP, or GFP alone.

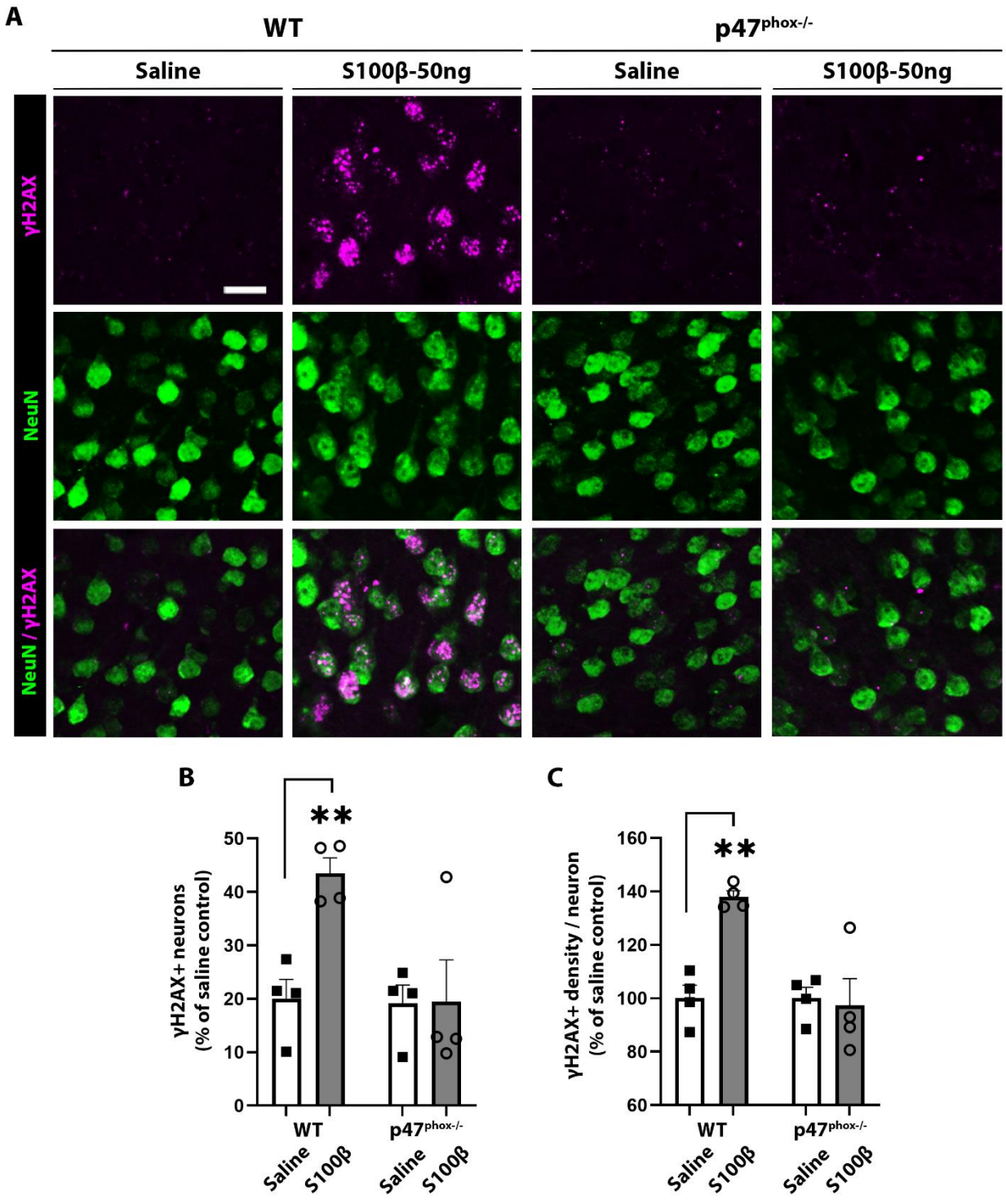

Figure S5, related to Figures 3 and 4. S100β induced neuronal oxidative stress. **(A)** Foci of γH2AX (magenta), which form at sites of DNA strand breaks, in nuclei of neurons immunostained with NeuN (green) in WT, but not p47$^{phox-/-}$ mice. Scale bar = 20 μm. Data are quantified in **(B)** as percent of neurons with detectable γH2AX signal and in **(C)** as mean integrated γH2AX signal density per neuron. Data are expressed relative to saline-injected controls. **p < 0.01 by Student's t-test. All data are shown as mean ± SEM.

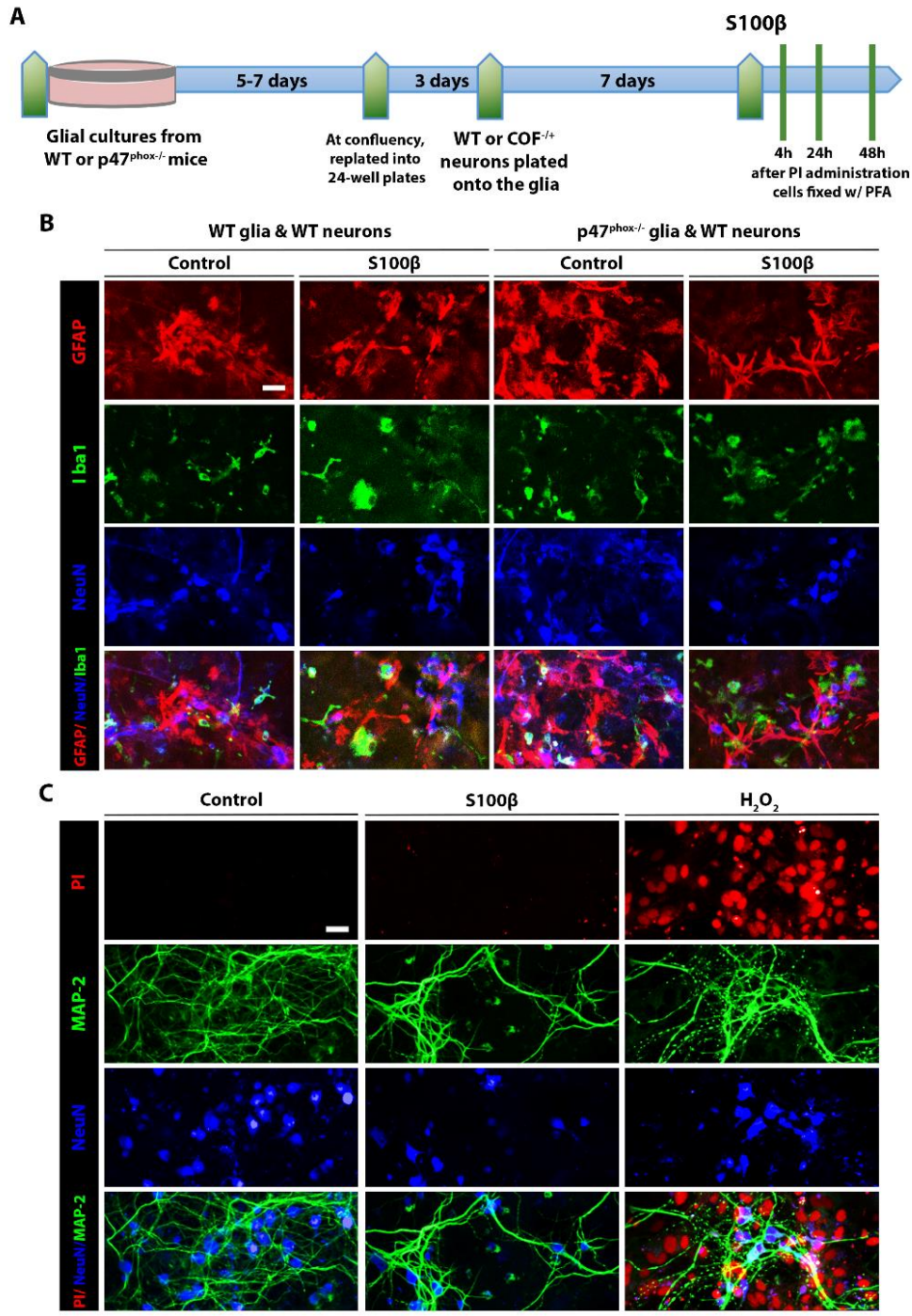

Figure S6, related to Figures 6 and 7. Characterization of cell culture preparations. **(A)** Schematic of co-culture preparations. **(B)** Immunolabeling for astrocytes (GFAP; red), microglia (Iba1; green) and neuronal somas (NeuN; blue) in co-cultures with or without 50 ng / ml S100β incubation for 48 hours. **(C)** Immunolabeling for neuronal somas and neurites with NeuN (blue) and microtubule-associated protein-2 (MAP-2; green) after propidium iodide (PI; red) incubation. 48 - hour incubations in 50 ng / ml S100β caused no detectable neuron death, as detected by PI permeability. H_2O_2 (10 μM) provides as a positive PI control. Scale bar = 20 μm. Representative of n = 3 co-culture preparations.

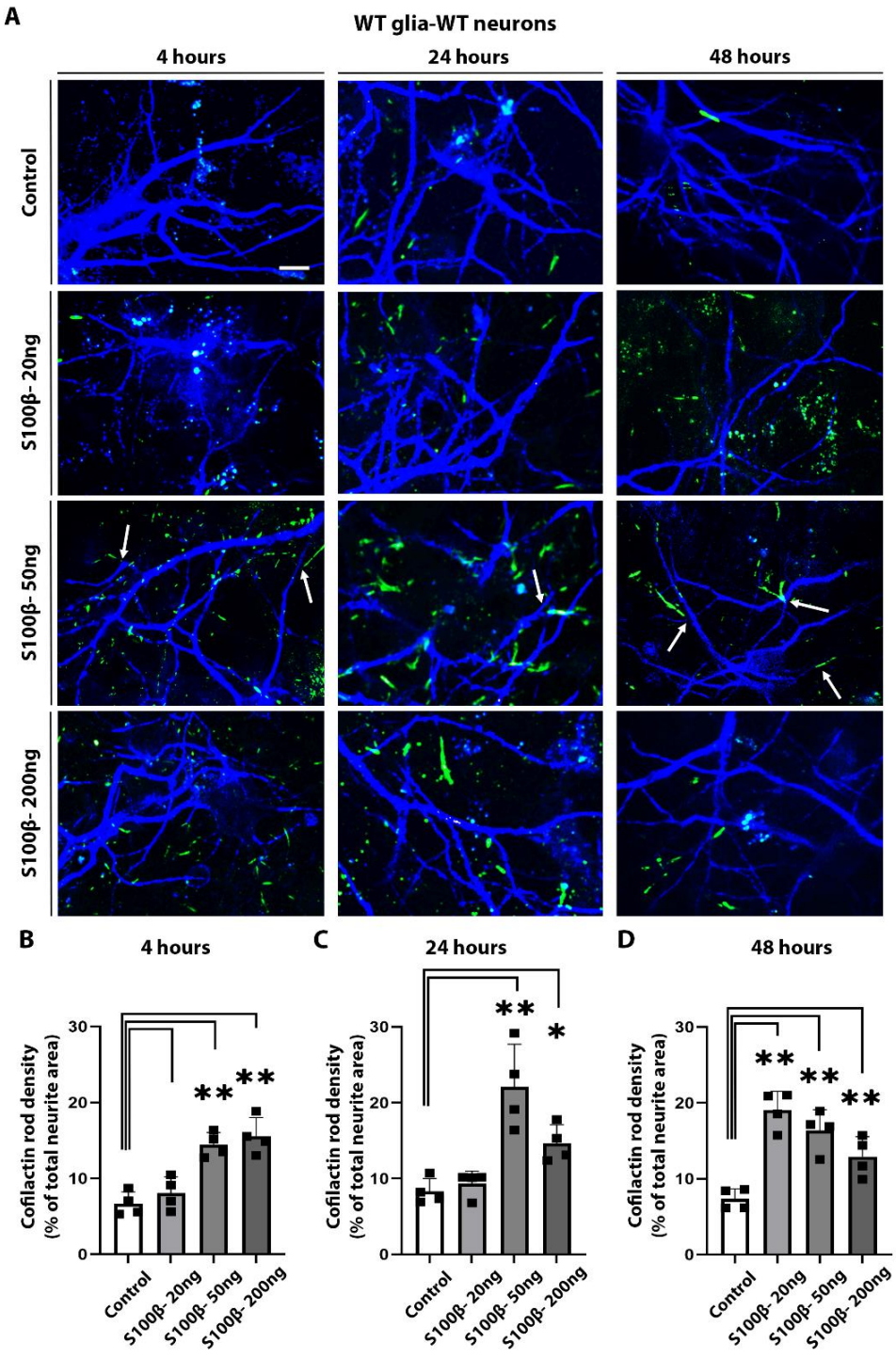

Figure S7, related to Figure 6. Dose- and time- response of S100β on CAR formation in neuron-glia co-cultures.

(A) Photomicrographs of co-cultures immunostained for MAP-2 (blue) and CAR (cofilin-1; green). Arrows identify examples of MAP-2 continuity disrupted by CAR formation. Scale bar = 10 μm. **(B-D)** CAR density expressed as percent of total neurite area. n = 4; *p, 0.05, **p < 0.01 vs. control by one-way ANOVA with Dunnett's test. All data are shown as mean ± SEM.

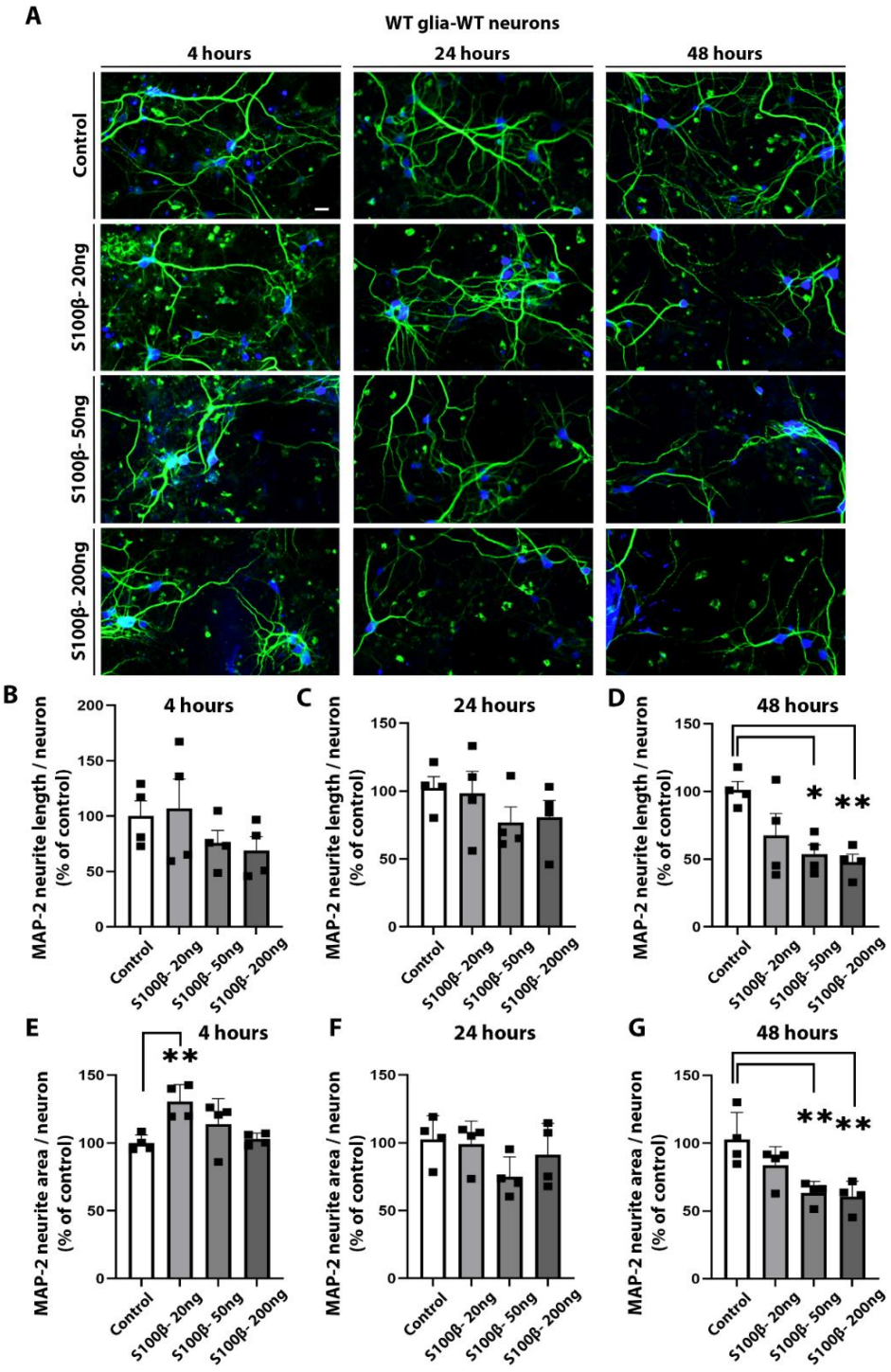

Figure S8, related to Figure 7. Dose- and time-dependent effects of S100β on neurite loss in wild-type neuron-glia co-cultures.

(A) Photomicrographs of co-cultures immunostained for MAP-2 (green) and NeuN (blue). Scale bar = 10 μm. **(B-D)** Neurite loss assessed by MAP-2 length / neuronal nucleus. **(E-F)** Neurite loss assessed by MAP-2 area / neuronal nucleus. Values are expressed relative to control wells prepared in parallel. n = 4; *p, 0.05, **p < 0.01 vs. by one-way ANOVA with Dunnett's test. All data are shown as mean ± SEM.

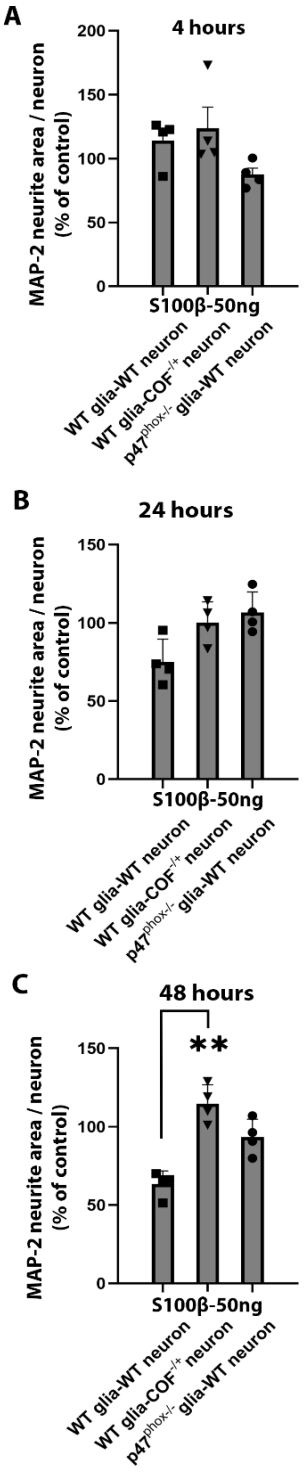

Figure S9, related to Figure 7. Neurite loss in neuron-glia co-cultures of mixed genotypes assessed by MAP-2 area. (A-C) Neurite area measurements corresponding to neurite length assessments in Figure 7. Data are shown as MAP-2 area / neuronal nucleus, expressed relative to the control condition of the respective co-culture type. n = 4; *p, 0.05, **p < 0.01 by one-way ANOVA with Dunnett's test. All data are shown as mean ± SEM.

References

S1. SMi, J., Shaw, A.E., Pak, C.W., Walsh, K.P., Minamide, L.S., Bernstein, B.W., Kuhn, T.B., and Bamburg, J.R. (2013). A genetically encoded reporter for real-time imaging of cofilin-actin rods in living neurons. PloS one *8*, e83609. 10.1371/journal.pone.0083609.